CHAPTER 30

Nanostructured Tin Dioxide Materials for Gas Sensor Applications

T. A. Miller, S. D. Bakrania, C. Perez, M. S. Wooldridge

Department of Mechanical Engineering, University of Michigan, Ann Arbor, Michigan 48109-2125, USA

CONTENTS

1. INTRODUCTION

1.1. Semiconductor Gas Sensors

Detection of pollutant, toxic, refining, combustible and process gases is important for system and process control, safety monitoring and environmental protection. Various methods can be used to accomplish gas sensing including gas chromatography, Fourier-transform infrared spectroscopy, chemiluminescence detectors, mass spectrometry, semiconductor gas sensors, and others. Gas sensors based on solid-state semiconductor materials offer considerable advantages in comparison to other gas sensing methods. Semiconductor sensors are inexpensive to produce, easy to miniaturize, rugged, reliable and can be designed to operate over a range of conditions including high temperatures. Semiconductor sensors can be produced in arrays to allow sensing of multiple species simultaneously and with advances in sensitivity; detectivity limits are approaching part-per-million (ppm) levels for some species.

Tin dioxide (also called stannic oxide or tin oxide) semiconductor gas sensors were first proposed [1] and patented in 1962 [2], and since then stannic oxide gas sensors have undergone extensive research and development. Tin dioxide (SnO_2) is the most important material for use in gas sensing applications. It is the dominant choice for solid-state gas detectors in domestic, commercial and industrial

ISBN: 1-58883-067-5
Copyright © 2006 by American Scientific Publishers
All rights of reproduction in any form reserved.

Functional Nanomaterials
Edited by Kurt E. Geckeler and Edward Rosenberg
Pages: 1–24

settings due to the low operating temperatures, high sensitivities, mechanical simplicity of sensor design and low manufacturing costs [2–5]. Millions of carbon monoxide (CO) alarms utilizing SnO_2 as the active sensing element have been produced and have demonstrated the long term (>10 years) dependable performance of tin dioxide sensors. In the past 15 years, considerable research has been conducted on understanding the chemical and electronic mechanisms that govern semiconductor sensor performance and on extending SnO_2 sensors to detection of other gases, including trace amounts of toxic gases [4, 6, 7, and references therein]. However, many challenges remain which prevent full realization of the diagnostic potential of SnO_2 sensors beyond carbon monoxide detectors, including the need to improve selectivity, sensitivity, stability and time response of the sensors.

There are several documents which provide excellent reviews of the scientific literature on SnO_2 sensors, including the works by Yamazoe [7], Ihokura and Watson [2], Hozer [8], Göpel and Schierbaum [6], and Park and Akbar [9]. The various physical and chemical mechanisms thought to be important in SnO_2 sensing systems are discussed in each of the review articles. The textbook by Ihokura and Watson [2] takes a comprehensive approach that includes archiving a large body of experimental data on the trends of SnO_2 sensor performance as a function of design and operating parameters, as well as material invaluable to the practicing engineer interested in sensor application. The work by Hozer [8] has a strong emphasis on practical fabrication and application of SnO_2 sensors to the detection of a broad range of gases. A detailed discussion of the electrical properties of SnO_2 sensors and schematic interpretations of sensor electronic, chemical, physical and geometric considerations are all provided in the manuscript by Göpel and Schierbaum [6]. Yamazoe [7] focuses on explanation of experimentally observed trends in terms of proposed electronic mechanisms for sensor response. The recent review by Park and Akbar [9] covers a spectrum of ceramic materials for sensor applications, with a primary focus on SnO_2 systems. Park and Akbar also provide extensive discussion of the fundamental principles involved at the gas-solid interface of the sensors. In this review, the emphasis is placed on the microstructural properties of the SnO_2 materials used in sensor applications, how the properties affect SnO_2 sensor function, and recent efforts to improve sensor performance, particularly through control of sensor microstructure.

Although our fundamental understanding of the chemical and physical mechanisms important in SnO_2 gas sensors has grown dramatically, improvements in sensor performance are still largely based on empirical studies. A clear trend that has emerged from these studies is the need for careful analysis of the micro-scale sensor properties (including physical and electronic properties) combined with simultaneous careful analysis of sensor performance. Establishing direct links between microstructure and performance is a vital step towards achieving sensors that are optimized at the nanometer level for specific sensing applications.

In the following sections, the chemical and physical mechanisms important in pure SnO_2 and doped SnO_2 gas sensors are briefly introduced. Methods that have been demonstrated for SnO_2 synthesis and the results of materials characterization of the pre-processed and post-processed SnO_2 powders used in gas-sensor applications are covered in Section 2. In Section 3, SnO_2 sensor architecture and fabrication technologies are briefly reviewed, and the results of studies to improve sensor performance and attempts to establish connections between microstructure and performance are presented. The work concludes with suggestions for areas of future research.

1.2. Mechanisms for Gas Sensing in Pure SnO_2 Sensors

It is well known that the performance of a SnO_2 sensor is directly related to the SnO_2 particle size, particle connections and compositional characteristics (i.e. the presence of additives) [6, 7, 10, 11]. For example, SnO_2 sensor performance (stability, sensitivity, selectivity, and response time) has been improved considerably by reducing the size of the SnO_2 particles used in the sensors to nanometer dimensions [7, 11–13] and/or by adding dopants (typically noble metals or other metal oxides) to the tin dioxide to create nanocomposite materials [6, 7, 12, 14–17]. Figures 1 and 2 show the results of Yamazoe's work [7] on the resistance and sensitivity of a SnO_2 sensor as a function of the SnO_2 crystallite size. The sensitivity is defined as the ratio of the resistance of the sensor in air to the resistance of the sensor in the test gas, i.e. $S = R_a/R_g$. Note the dramatic increase in the sensor resistance and sensitivity for crystallite sizes less than ~6 nm.

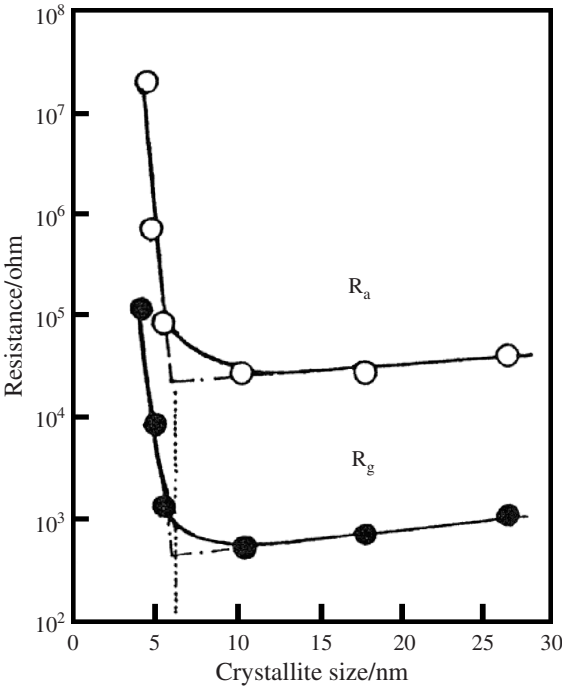

Figure 1. Experimental data showing the effect of SnO_2 crystallite size on sensor resistance for undoped tin oxide generated using sol–gel synthesis processing. Data are shown for sensor response to 800 ppm of H_2 in air at a sensor operating temperature of 300 °C. Reprinted with permission from [7], N. Yamazoe et al., *Sens. Actuators B* 5, 7 (1991). © 1991, Elsevier.

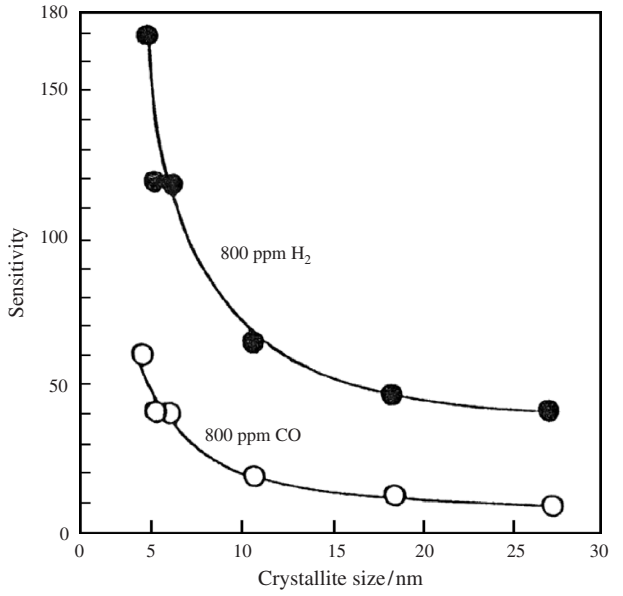

Figure 2. Experimental data showing the effect of SnO_2 crystallite size on sensor sensitivity (undoped tin oxide generated using sol–gel synthesis processing). The sensitivity is defined as the ratio of the resistance of the sensor in air to the resistance of the sensor in the test gas, i.e. $S = R_a/R_g$. Data are shown for sensor response to 800 ppm of H_2 in air, and 800 ppm of CO in air at a sensor operating temperature of 300 °C. Reprinted with permission from [7], N. Yamazoe et al., *Sens. Actuators B* 5, 7 (1991). © 1991, Elsevier.

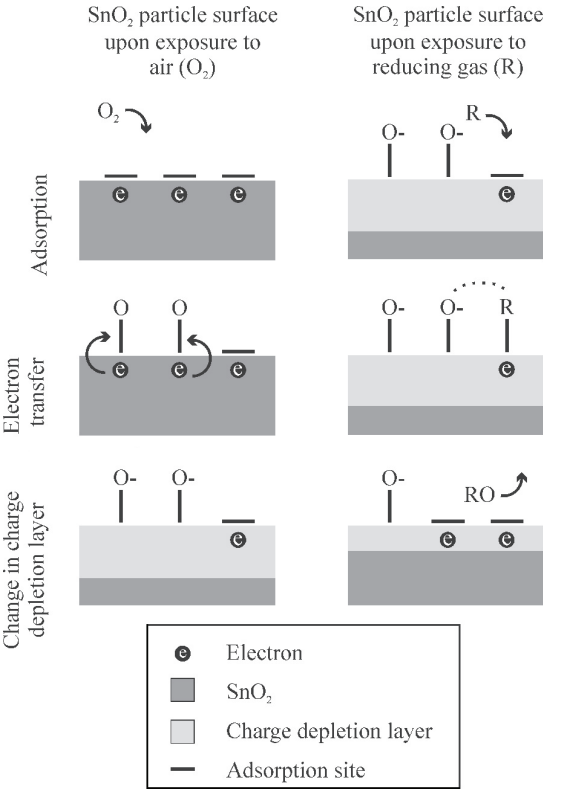

Figure 3. Schematics indicating the mechanisms leading to SnO_2 sensor response to oxidizing and reducing gases.

Tin dioxide is an *n*-type semiconductor, where the sensor conductivity increases in the presence of a reducing gases (such as CO), and decreases in the presence of an oxidizing gas (such as O_2). SnO_2 sensor response is due to surface interactions between the tin oxide and the surrounding gases. The general steps involved in sensor response upon exposure to air and to a reducing gas, *R*, are shown in Figure 3. As shown in the column on the left of Figure 3, oxygen from the air is adsorbed onto the surface of the SnO_2. Electrons from the surface region of the SnO_2 are transferred to the adsorbed oxygen, leading to the formation of an electron-depleted region near the surface of the SnO_2 particle. The electron depleted region, also called the space-charge layer, is an area of high resistance and the core region of the particle, where electron densities are high, is an area of relatively low resistance. The form of the adsorbed oxygen (either molecular or atomic) depends on the temperature of the sensor, where O_2^- species have been observed at lower temperatures (below 175 °C) and O^- and O^{2-} species have been observed at higher temperatures (above 175 °C) [18, and references therein].

As shown in the column on the right of Figure 3, when exposed to a reducing gas like CO, surface reactions such as

$$CO + O^-_{ads} \rightarrow CO_2 + e^-$$

and

$$2CO + O^-_{2,\,ads} \rightarrow 2CO_2 + e^-$$

release electrons back to the SnO_2 and lead to a decrease in the resistance of the space charge layer.

It is important to note that *n*-type semiconductor materials such as SnO_2 have relatively few oxygen adsorption sites available (e.g. compared to noble metals) due to the development of potential barriers on the particle surface [19]. In addition, the fraction of surface sites occupied of those available on the surface of the SnO_2 is low (<1%) [9]. Consequently, incorporating species which have a comparably higher number of adsorption sites with high fractional occupancy in the SnO_2 sensing material can have a significant impact on the sensor performance, as discussed further in Section 1.3.

Crystallite size effects on sensor performance, such as the trends observed in the data shown in Figures 1 and 2, are generally explained in terms of the relative values of the characteristic dimensions of the connection between adjacent particles (the neck width) and of the thickness of the space charge layer. The thickness of the space charge layer is typically indicated by the Debye length, L_D, of the electrons in the SnO_2 [20–22]. Figure 4 shows the various regimes that are of interest in SnO_2 sensors based on the relative values of the neck width and the Debye length. Park and Akbar [9] propose that the intergranular contacts between SnO_2 particles can be classified into three categories: open neck, closed neck and Schottky contact-type connections. Specific conductance models are associated with each category of interparticle connection. Figure 4 includes reference to the corresponding interparticle models of Park and Akbar, as well as reference to the regimes based on characteristic grain and particle sizes proposed by Yamazoe [7].

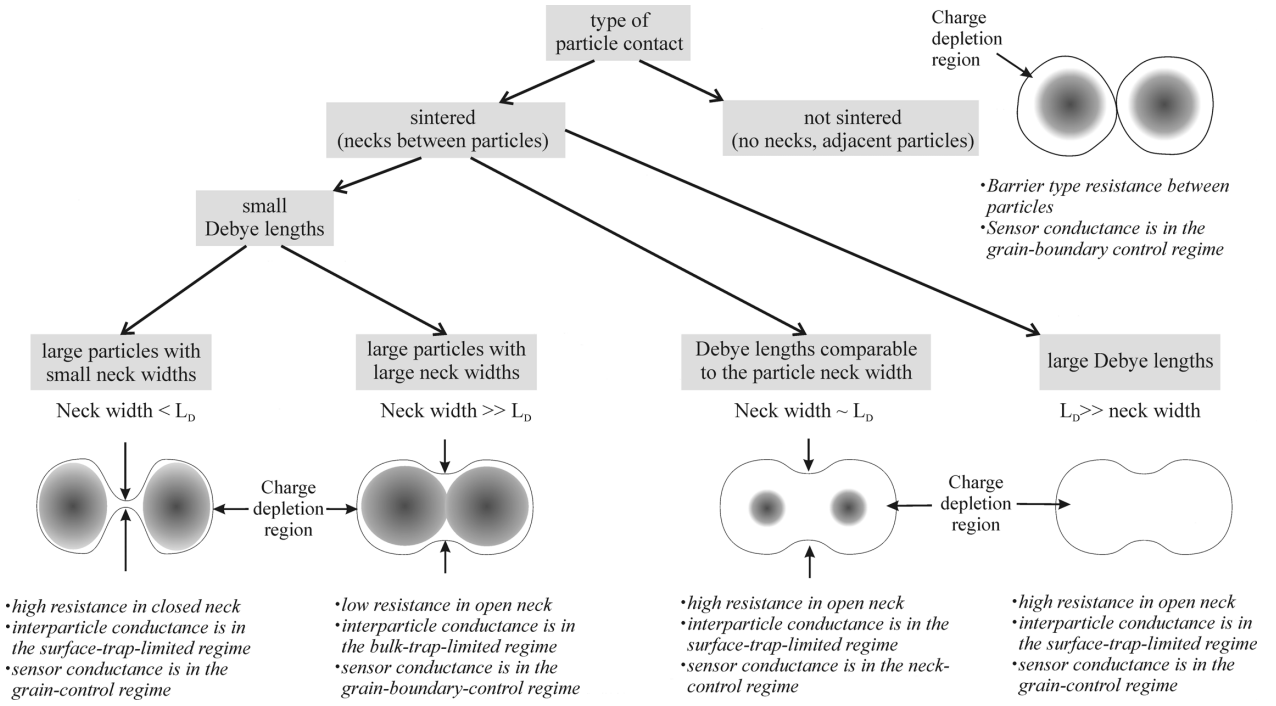

Figure 4. Schematic indicating the conductance mechanisms important in the various SnO_2 crystallite size regimes, relative to the SnO_2 electron Debye length, L_D. For reference, the Debye length of undoped SnO_2 has been previously estimated as ~3 nm. Below each particle pair, the dominant mode of resistance is listed first, the interparticle conductance mechanisms as per the criteria proposed by Park and Akbar [9] is listed second, and the sensor conductance regime (assuming a sensor consisting entirely of that category of particle connections) is listed third as per the criteria specified by Yamazoe [7].

The dramatic dependence of sensor sensitivity on SnO_2 particle size can be understood by considering the size regimes outlined in Figure 4. As the crystallite dimension decreases relative to the Debye length of the electrons in the SnO_2, the sensor conductance becomes dominated by the high resistance of the interparticle necks. Under these conditions, the sensor sensitivity is a very strong function of the size of the necks between the particles. Yamazoe found the size of the necks is approximately proportional to the particle size (neck width $\cong 0.8\ d_p$, where d_p is the average SnO_2 crystallite size). Thus, the resistance of the sensor increases as the SnO_2 particle size decreases when $d_p \ll L_D$. Yamazoe refers to this as the grain-control regime [7], and Park and Akbar describe the interparticle conductance for this regime using an open neck/surface trap limited conductance model [9].

Unfortunately, SnO_2 sensors are not typically composed of one category of particle contact, or modeling and sensor design would be greatly facilitated. To compound the challenge, SnO_2 sensors are often porous. The porosity of the SnO_2 can also play a role in dictating the response mechanism of the sensor. Figure 5 is a schematic depicting the various interparticle connections, grain boundaries and electrode/particle contacts that can be found in a typical SnO_2 film sensor. As discussed at length in the review by Göpel and Schierbaum [6], the configuration of the sensor can lead to systems where the sensor resistance is dominated by one type of contact, such as the electrode/SnO_2 interface for example. More likely, however, a percolation model is required for accurate representation of the electron flow in the sensor, and as seen in Figure 5, the relevant spatial dimensions of a tin oxide sensor often span orders of magnitude. The recent work by Barsan and Weimar [18] provides a thorough and detailed discussion of their model development to represent the various porosities, particle sizes and degrees of particle connectivity that are encountered in SnO_2 sensors. In particular, the authors strive for achieving a model based on the fundamental physical, chemical and electrical mechanisms important in metal oxide sensors while still retaining flexibility to use the models for practical sensor design.

1.3. Mechanisms for Gas Sensing in SnO_2 Sensors with Additives

Decreasing the SnO_2 crystallite size can dramatically improve sensor sensitivity; however, the small dimensions required are difficult to achieve in a practical sensor. For example, sensors composed of nanosized SnO_2 crystallites with $d_p < 10$ nm can have poor mechanical strength [7], and heat treatment processes tend to increase the characteristic SnO_2 crystallite size (which is discussed further in Section 2). Fortunately, the use of additives in the SnO_2 sensing material can have an even more marked effect on sensor performance than SnO_2 particle size, as seen in Figure 6.

Additives can have several effects on the SnO_2 properties important to gas sensing applications, including inhibiting SnO_2 grain growth, modifying the electron Debye length and modifying the gas-surface interactions. Heat treatment

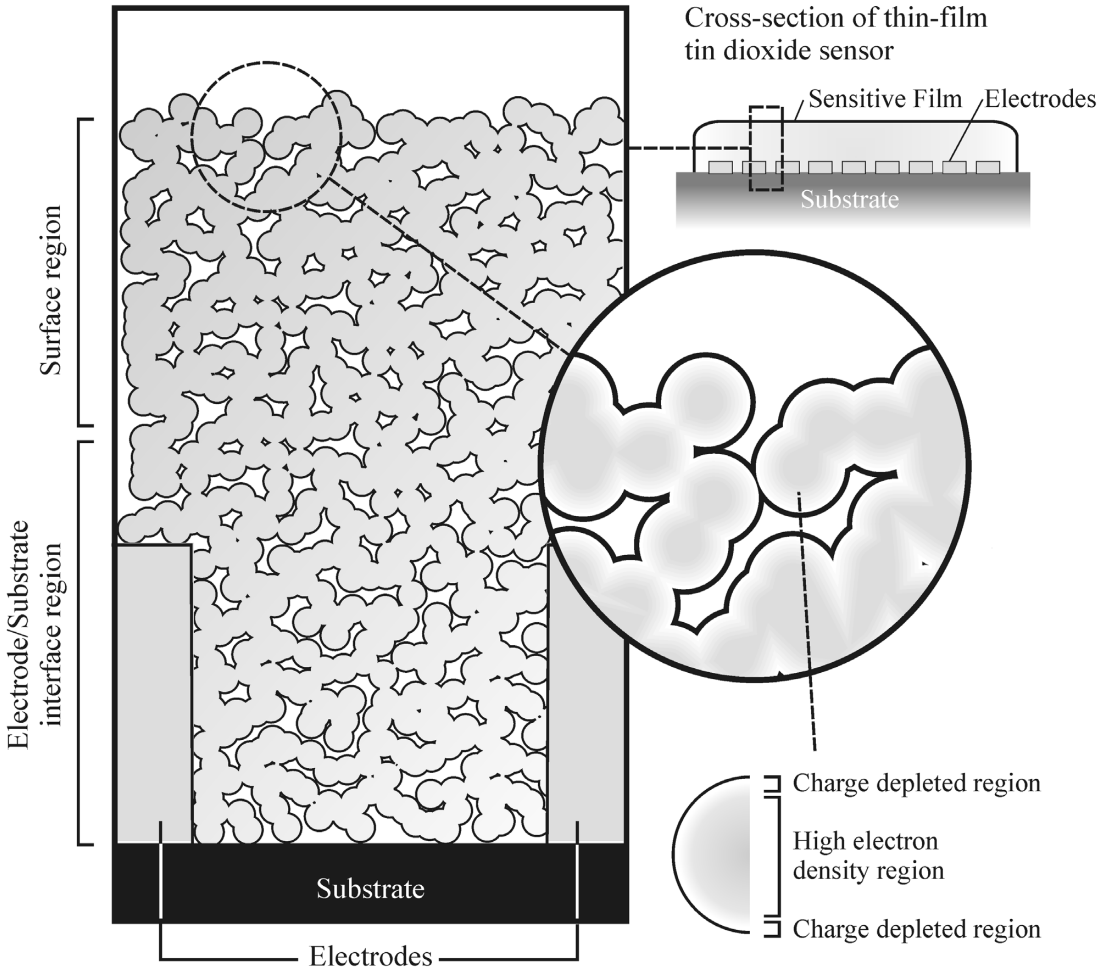

Figure 5. Schematic indicating the interparticle connections, grain boundaries, and particle/electrode contacts present in a typical porous SnO_2 film sensor.

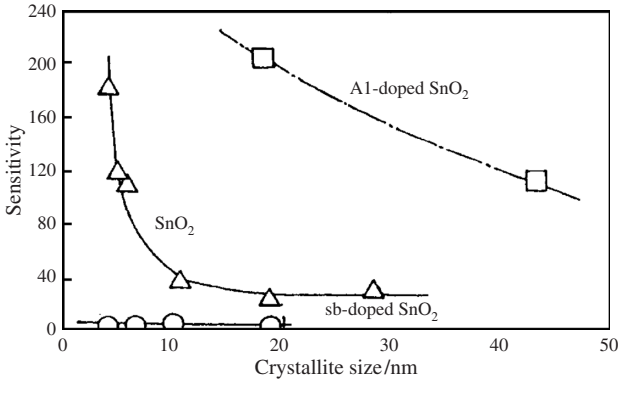

Figure 6. Experimental data showing the effect of additives on SnO_2 sensor sensitivity as a function of SnO_2 crystallite size (sol–gel generated materials). Data are shown for sensor response to 800 ppm of H_2 in air at a sensor operating temperature of 300 °C. Reprinted with permission from [7], N. Yamazoe et al., *Sens. Actuators B* 5, 7 (1991). © 1991, Elsevier.

processes are integral to sensor fabrication [2], and these processes result in significant restructuring of the SnO_2 crystallites. Additives can limit the extent of the SnO_2 coalescence. Results of grain inhibitor studies of SnO_2 additives and the effects of heat treatment on the characteristic SnO_2 crystallite size are presented in Section 2.

Regarding modifications to the SnO_2 electron Debye length, L_D, Yamazoe [7] suggests that the data shown in Figure 6 are consistent with estimated changes in L_D for the aluminum and antimony additives examined. Compared to the unaltered Sn^{4+} lattice structure, Al^{3+} and Sb^{5+} should lead to larger and smaller SnO_2 electron Debye lengths, respectively. Larger Debye lengths, and hence space charge layers, shift the sensitivity response curve to larger SnO_2 crystallite particle sizes, as seen for Al.

Additives can also change the gas-surface interactions of a tin oxide sensor. Two mechanisms have become widely accepted for describing the chemical and physical processes important in SnO_2 sensors with additives: the electronic and the catalytic mechanisms. Figure 7 shows the general steps involved with the two mechanisms. In the electronic mechanism (shown in the column on the left of Fig. 7), also called

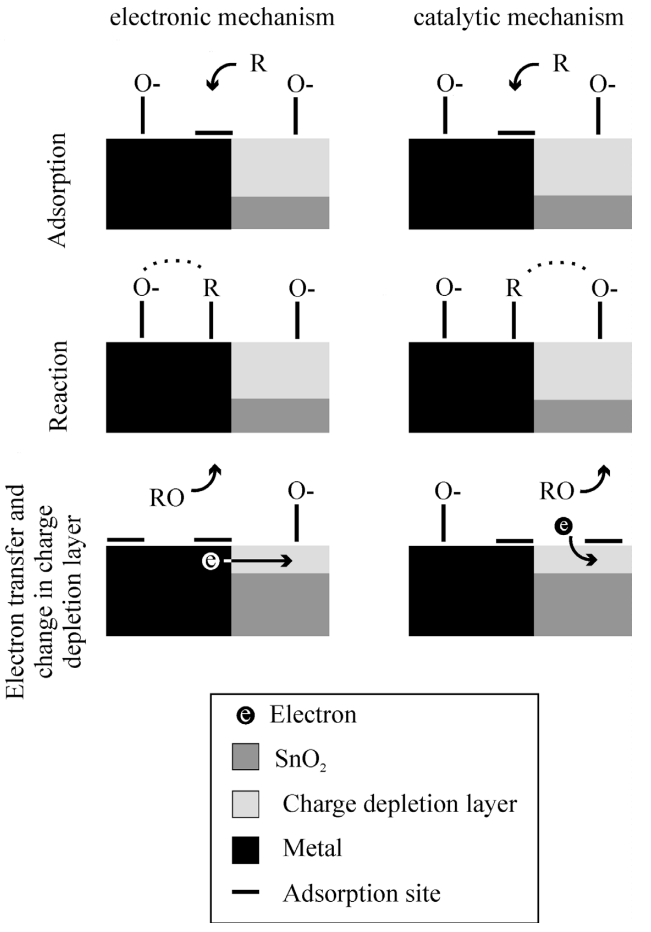

Figure 7. Schematic indicating the general steps involved in the electronic and catalytic mechanisms active in SnO_2 sensors with metal additives. *R* represents a reducing gas.

the Fermi energy control mechanism, a reducing gas reacts on the surface of the metal additive, releasing an electron which is transported to the SnO_2. The change in the electron density near the surface of the SnO_2 leads to a decrease in resistance. In the catalytic mechanism, also called the chemical mechanism or spill-over mechanism, the metal additive acts as a catalyst where the reducing gas is transported to the SnO_2 surface. As shown in the sequence in the column on the right of Figure 7, the reducing gas reacts with the oxygen adsorbed on the surface of the SnO_2, thus releasing an electron directly to the charge depleted region of the SnO_2 particle. The primary difference between the electronic and catalytic mechanisms is the particle being transported between the additive and the SnO_2. Electron transfer occurs in the electronic model and atom transfer occurs in the chemical model.

The general descriptions of the electronic and catalytic mechanisms found in the literature are largely consistent. Yet, there is considerable uncertainty in the detailed representation of the models. For example, hydrogen decomposition and transport on metal catalysts has been observed and is well documented in the literature [19, and references therein]. Oxygen adsorption and transport on the surface of SnO_2 metal additives has also been proposed as a means to explain changes SnO_2 sensor properties that occur when using metal additives [19]. However, there are few studies which consider, let alone quantify, adsorption and transport of both reducing and oxidizing species in doped SnO_2 sensors.

Another good example of the limitations of the electronic and catalytic models is found in the recent experimental study by Montmeat et al. [23]. The authors conducted an investigation of the effects of gold on SnO_2 sensor response where they used a novel test facility. In the new sensor testing facility, specific regions of the sensor (the electrodes and the region between the electrodes) could be isolated from exposure to the target gas. They found the sensor response was dominated by interaction with the gold electrodes, and the results could not be explained in terms of either the electronic or catalytic mechanisms. Montmeat et al. proposed a new form of highly ionized adsorbed oxygen species may be formed at the boundary between the gold metal particle, the SnO_2 particle, and the gas. Thus a new mechanism may be necessary to represent the sensor properties at these edge or border regions.

Ultimately, the fundamental principles underlying how the additives lead to the enhancements of SnO_2 sensor performance are still not well understood. Advances are also complicated by the fact that the additives probably play multiple roles in augmenting the sensor performance. For example, metal additives are likely to be present in multiple morphologies (e.g., dispersed into the SnO_2 matrix and present as discrete particles), as has been noted by several researchers [7, 24]. The dispersed additives can change the electron Debye length, while the discrete particles simultaneously affect the gas-surface properties. Consequently, the methods for how to select an additive and design the combined sensor/additive morphology remain a challenge.

2. SNO_2 SYNTHESIS METHODS AND MATERIALS CHARACTERIZATION RESULTS

2.1. Pure SnO_2

Nanosized tin oxide particles can be generated using a variety of synthesis techniques including sol gel processing [12, 16, 17], chemical vapor deposition [25], wet chemical deposition [26, 27], sputtering methods [10, 20], flame synthesis [28–30], gas phase condensation [5], pulsed laser ablation [54], and mechanochemical processing [31]. Some key manufacturing considerations of the synthesis methods include scalability for industrial production, repeatability of the SnO_2 properties, purity of the SnO_2 product materials, toxicity and handling considerations of the SnO_2 precursor materials, continuous versus batch processing, cost of materials and procedures required, and the number, complexity and waste associated with the sensor fabrication steps required for the SnO_2 starting materials. Important characteristics of some representative methods demonstrated for synthesis of undoped SnO_2, including the reactant precursor materials used, the form of the SnO_2 produced and the average SnO_2 crystallite size, are provided in Table 1. As an indication of the performance of the materials, sensitivity data are also provided (where available) in Table 1.

Table 1. Representative synthesis methods, material characteristics and corresponding sensor sensitivity (where available) for undoped SnO_2 systems.

SnO_2 synthesis method	SnO_2 precursor	Preparation methods referenced in synthesis procedure	Form of SnO_2 produced	SnO_2 crystallite size	Sensitivity (Resistance ratio, R_a/R_g, at specified operating temperature and mole fraction of target gas)	Ref.
Sol–gel processing	Hydrated $SnCl_4$	Hydrothermal treatment, dried, calcined, ground	Powder	5 nm	• 170 at 300 °C, 800 ppm of H_2	[11]
	Tin(II)2-ethylexanoate	Solution, dried, calcined	Powder	10–40 nm	• 3.1 at 300 °C, 100 ppm of CO[a]	[59]
	Granulated Sn	Sol gel, dried, ground, calcined	Powder	3–6 nm	N/A	[33]
Sputtering	Sn	Low-pressure, sputtered as film, annealed, both SnO_2 and SnO films	Film	N/A	N/A	[12, 10]
Combustion synthesis	$Sn(CH_3)_4$	Gas-phase, low pressure flame	Powder	5–13 nm	N/A	[28]
	Tetra-*n*-butyltin	Gas-phase, low pressure flame	Film	N/A	N/A	[30]
	$SnCl_4$ in propane 1,2 diol	Spray pyrolysis	Film	20–40 nm	• 3.3 at 200 °C, 3200 ppm of C_2H_5OH	[60]
	$Sn(CH_3)_4$	Gas-phase, atmospheric pressure flame	Powder	8–20 nm	N/A	[35, 61]
Pulsed laser ablation	SnO_2	Deposited onto Si substrate, annealed	Film	20–60 nm	• 1.2 at 400 °C, 30 ppm of CO[a]	[54]
Gas-phase condensation	SnO	Low-pressure, evaporated, condensed, calcined	Powder	5–15 nm	N/A	[5]
Co-precipitation	$Sn(OH)_4$ precipitated from $SnCl_4$	Precipitated, washed, crushed, calcined	Powder	9 nm	• 0.3 at 400 °C, 1000 ppm of CH_4	[62]
Micro-emulsions	$SnCl_4$ pentahydrate	Water-in-oil emulsion system, calcined	Powder	30–70 nm	N/A	[63]
Wet chemical deposition	$SnCl_2$	Wet deposition, oxidation	Film	~3–30 nm	• 1.1 at 200 °C, 3000 ppm of H_2	[27]
Chemical vapor deposition	$SnCl_4$	Plasma enhanced chemical vapor deposition	Powder	10 nm	• 8.0 at 445 °C, 1000 ppm of CO	[64]
Mechano-chemical processing	$SnCl_2$	Milled, heat-treated and washed to remove NaCl by-product	Powder	5–30 nm	N/A	[31]

[a]Sensitivity given as a conductance measurement, where $S = (G - G_o)/G_o$.

Additional discussion of SnO_2 sensor performance can be found in Section 3.

Most of the synthesis methods are competitive with respect to the SnO_2 crystallite size, with the smallest particle size being about 5 nm. However, the average SnO_2 crystallite size associated with the material synthesis technique is not always representative of the average crystallite size of the final sensor product. Most of the sensor fabrication methods (which are discussed further in Section 3) require some form of heat treatment, e.g. sintering or calcination. The SnO_2 particle sizes can and usually will grow during the high-temperature sensor fabrication processes. The extent of the growth is both time and temperature dependent [7].

Empirical studies have long been the basis for developing improvements in stannic oxide sensor performance. These have shown that the microstructural properties (both physical and electronic) of the tin oxides affect SnO_2 sensor performance. A variety of analytical techniques have been used to study the particles and their properties, which in turn can hopefully be used to link microstructure to performance and lead to better design and optimization of SnO_2 sensors. Some commonly used analytical techniques include transmission electron microscopy (TEM), scanning electron microscopy (SEM), energy dispersive spectroscopy (EDS), X-ray diffractometry (XRD), X-ray photoelectron spectroscopy (XPS), and specific surface area analysis (N_2 adsorption isotherms using BET theory). Transmission electron microscopy provides an imaging technique that can be used to determine grain sizes, particle morphology, lattice parameters, and overall particle structure. Scanning electron microscopy imaging is useful for examining film structure, sensor component connections and other larger scale features. Energy dispersive spectroscopy is an analytical technique which can be associated with either TEM or SEM and allows for elemental speciation of the sample. X-ray diffraction typically provides information on the crystalline phase of a larger sample size compared to the electron microscope methods, and XRD can be used for determination of an average crystallite size. X-ray photoelectron spectroscopy allows for the examination of the chemical composition of surfaces. Nitrogen adsorption analysis can give specific surface areas of a sample which can be correlated to porosity as well.

In the following paragraphs, analytical results of various studies that provide insight into the microstructure, phase, composition, morphology and other characteristics of undoped SnO_2 sensor materials are presented. Because the synthesis and fabrication methods dictate these properties, the results are presented for each of the representative synthesis methods listed in Table 1. Materials characteristics that are common to most of the pure SnO_2 synthesis techniques are presented first.

As seen in Table 1, the fabrication of SnO_2 material can lead to a powder form or directly to a film form. The most widely used technique for the manufacture of tin oxides for sensor applications is the sol–gel method which usually results in a powder product. Sol–gel synthesis techniques can be relatively inexpensive (depending in part on the precursors used), and they typically produce nanosized SnO_2 particles with narrow size distributions and good homogeneity. However, the SnO_2 particles may exhibit chlorine contamination when tin chlorides are used as the sol–gel reactant precursor [32, 33], which requires additional processing to purify. Recently, Zhang and Gao [32] have demonstrated an improved sol–gel processing method which yields very small SnO_2 materials that are relatively monodisperse (2.8–5.1 nm in size) and free from chloride impurities.

Tin oxide nanoparticles typically exhibit the same general morphologies regardless of the synthesis method. Figure 8 shows TEM images of representative sol–gel-generated [34] and flame-generated powder SnO_2 materials. The sol–gel powder was hydrothermally treated and exhibited an average particle size of less than 6 nm with a narrow size distribution of 5–8 nm. The tin oxide particles were produced in our facility using a combustion synthesis technique (the synthesis method is described in detail in Hall et al. [35, 61]) and have a slightly larger average crystallite size ($d_{p,\,\mathrm{avg}} = 11$ nm, based on TEM imaging) with a broader size distribution (for typical synthesis conditions) [35]. The characteristic morphology of the sol–gel and flame-generated materials is similar, where distinct primary particles are visible with some necking between particles. Figure 9 shows additional TEM images of the tin dioxide particles produced by combustion synthesis. The crystalline structure of the SnO_2 nanoparticles and typical interparticle connections can be seen in the Figure 9 images. Note the lattice fringes of the SnO_2 crystallite are clearly visible in the high resolution TEM image Fig. 9b).

The tin oxide powder used in gas sensor applications is most often the tetragonal cassiterite phase of SnO_2. A representative XRD pattern of flame-generated SnO_2 powder created for sensor applications is shown in Figure 10. The Miller indices are provided in the Figure and all peaks index to the cassiterite phase with no detectable features from other phases or materials. Note that the powders exhibit broad peaks consistent with nanosized powder materials. As mentioned above, XRD patterns can also be used to estimate the average crystallite size using Scherrer's relations. XRD provides the advantage of averaging over a much larger sample size compared to TEM image analysis, where

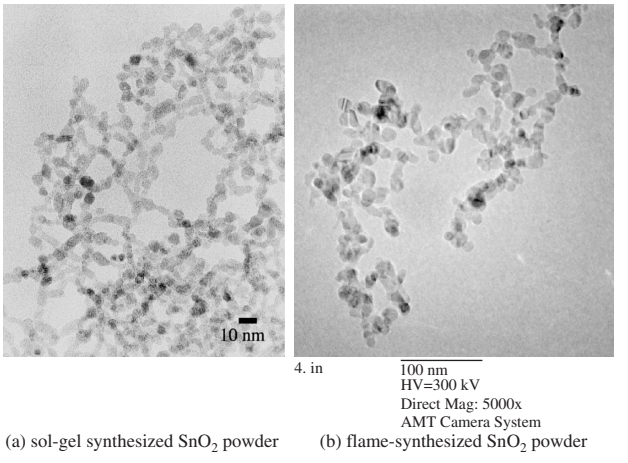

(a) sol-gel synthesized SnO_2 powder (b) flame-synthesized SnO_2 powder

Figure 8. Transmission electron micrographs of sol–gel generated and flame-generated SnO_2 particles (no additives) used in sensor applications. The size bar in Figure 8a represents 10 nm. The size bar in Figure 8b represents 100 nm. Figure 8a is reprinted with permission from [34], Baik et al., *Sens. Actuators B* 63, 74 (2000). © 2000, Elsevier.

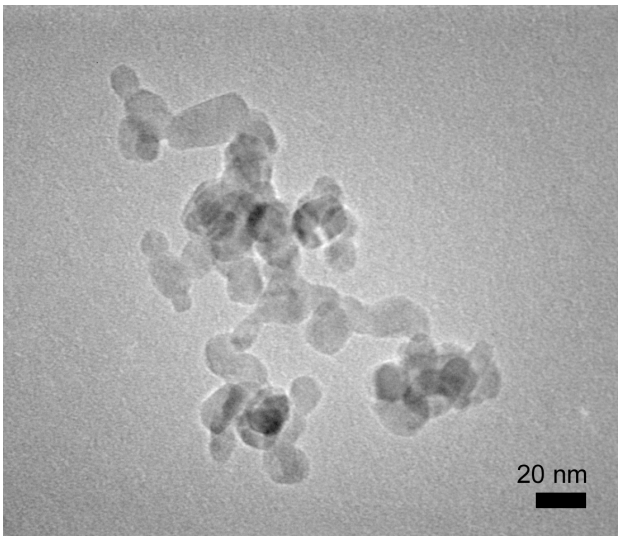

(a)

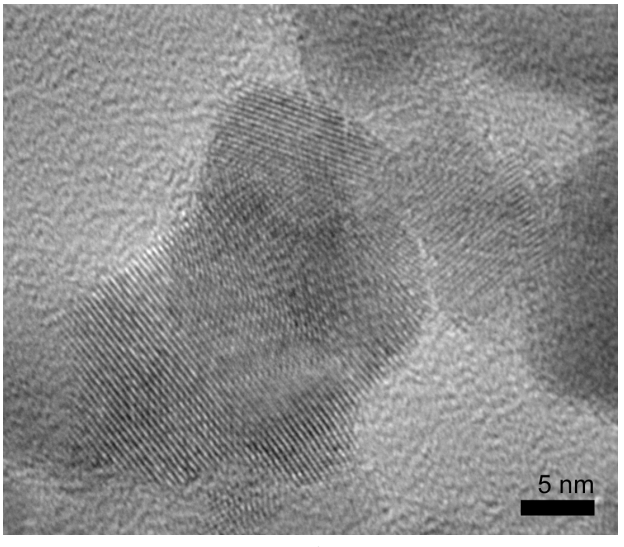

(b)

Figure 9. TEM images of flame-generated undoped SnO_2 particles showing the interparticle connections and the crystalline nature of the particles. The size bars in the images are (a) 20 nm and (b) 5 nm.

large particle counts are required to obtain statistically accurate values of the average SnO_2 particle size.

As mentioned earlier, the sensor fabrication steps subsequent to the powder synthesis can modify the characteristic dimensions of the SnO_2 crystallite size. For example, in the work by Siciliano et al. [16], who used sol–gel techniques to fabricate 100 nm SnO_2 films, the crystallite size grew from 3–6 nm to 12 nm upon high-temperature annealing. Ihokura and Watson provide additional examples quantifying SnO_2 crystallite growth at various temperatures and residence times [2]. Due to the key role SnO_2 particle size plays in sensor performance, limiting particle growth is a significant area of research and development. Advances in the SnO_2 synthesis methods demonstrated by Yamazoe and co-workers [11, 34, 36, 37, 72] have improved the resistance of the SnO_2 nanoparticles to coalescence and growth.

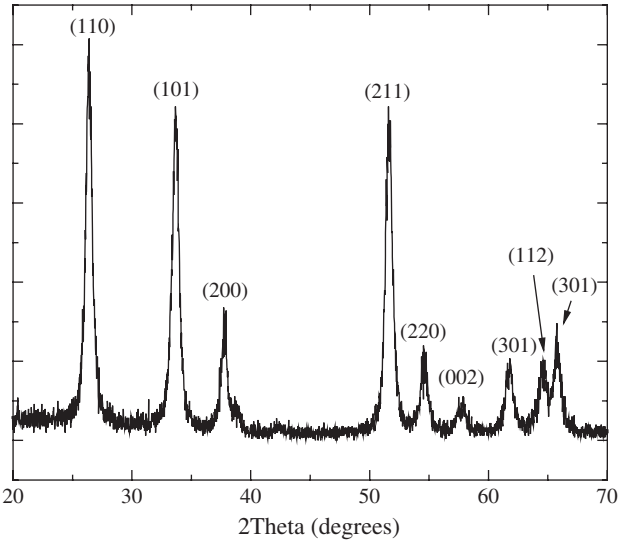

Figure 10. XRD spectra of undoped flame-generated SnO_2 powder created for gas sensor applications. The Miller indices of the tetragonal phase of SnO_2 (cassiterite) are noted in the Figure.

Yamazoe's group has pioneered the use of hydrothermal processing for synthesis of SnO_2 nanoparticles that experience limited growth even during high-temperature calcination. For example, in the work by Sakai et al. [37], a sol–gel SnO_2 powder with average particle size of 6 nm was spin-coated onto an alumina substrate yielding a uniform thin film with a 300 nm thickness. After calcination at 600 °C, the film retained an average grain size of about 7 nm, as well as good uniformity and connectivity of the crystallites (see Fig. 11).

The spin coating process itself is not without challenges affecting the SnO_2 connectivity and conductivity. For example, Figure 12 presents SEM images of sequential depositions of spin coating layers at three sol concentrations. As the film thickness increases with successive layering, the films begin to exhibit large-scale discontinuities and poor connectivity and uniformity. Some SnO_2 synthesis methods can be used to fabricate either SnO_2 powders or SnO_2 films directly, thus avoiding potential complications with spin coating. However these methods have other associated difficulties to overcome, as seen in the synthesis techniques discussed next.

Combustion synthesis techniques are robust synthesis methods that have been demonstrated for producing a range of nanostructured powder and film materials [38–40]. Combustion synthesis can be used to generate high-purity products with controlled particle size, particle size distribution, morphology (e.g. degree of agglomeration) and composition [38, 39]. Additionally, Laine and co-workers [41, 42] have demonstrated the scalability of combustion synthesis methods for high powder production rates, on the order of g/hr to kg/hr. Gas-phase combustion synthesis (where the reactant precursors are in the gas-phase) can be used to produce SnO_2 nanopowders or films with particle sizes ranging from 5–20 nm (see Table 1). Flame spray pyrolysis (where the reactant precursors are usually a liquid solution) has also been used for SnO_2 powder and film formation with particle sizes ranging from 8–15 nm [43] and 20–40 nm [60]. Combustion-generated particles are typically

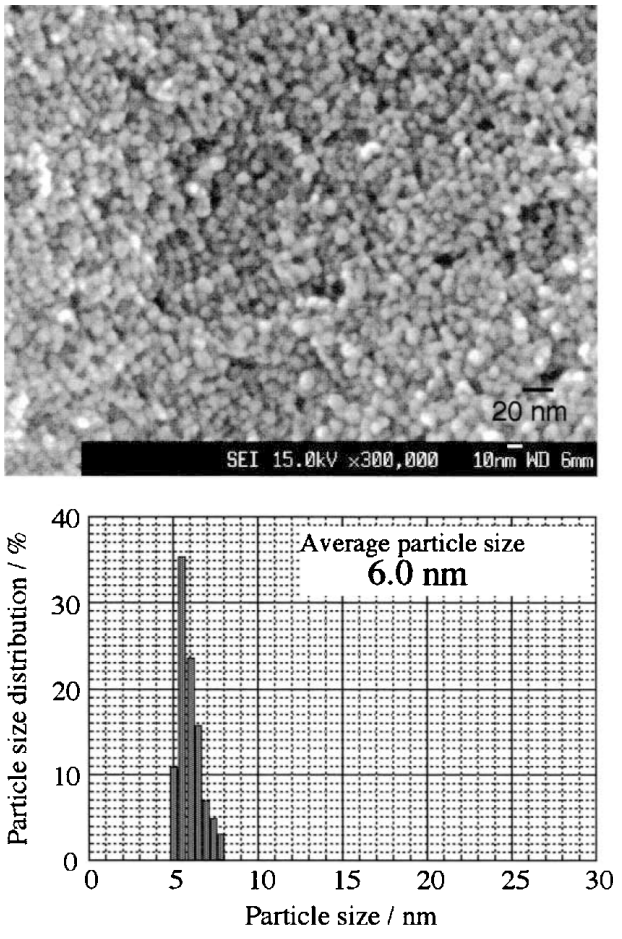

Figure 11. Field-emitting SEM image of a thin film (300 nm thickness) created via spin coating undoped sol–gel SnO_2 powder onto an alumina substrate. The size bar in the top panel represents 20 nm. The corresponding SnO_2 particle size distribution determined from analysis of the SEM image is shown in the lower panel. Reprinted with permission from [37], Sakai et al., *Sens. Actuators B* 77, 116 (2001). © 2001, Elsevier.

polydisperse with log-normal particle size distributions [28, 35, 44], and the average particle size can be controlled through the burner operating conditions [29]. As with some sol–gel methods, combustion-generated SnO_2 materials may suffer from chlorine contamination depending on the precursor used [60]. However, combustion methods are one of the few techniques which have been demonstrated to directly produce both thick and thin SnO_2 films [30].

Other fabrication techniques that can directly deposit a SnO_2 film onto a substrate include sputtering, pulsed laser ablation and gas-phase condensation methods. Sputtering is the most prevalent method used for direct production of SnO_2 thin film sensors. Sputtering can result in very thin, uniform and well-controlled film properties. In addition, Min and Choi [45] have demonstrated ion beam sputtering for production of SnO_2 thin films with good adhesive properties and excellent long term stability. Sputtering also offers great flexibility when creating sensors with controlled compositional structures, such as sensors which incorporate doping materials [46, 47] or sensitizing layers [48]. Although there are numerous studies on the effects of the sputtering

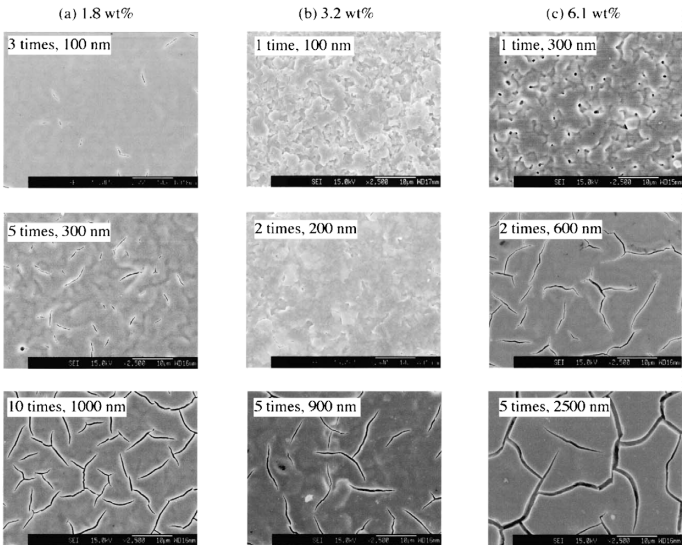

Figure 12. SEM images (top view) of undoped-SnO_2 thin films spin-coated with various concentrations of SnO_2 in the sol. Images of sequential coatings onto the substrate are provided in each column. The size bar in each image represents 10 μm. Reprinted with permission from [37], Sakai et al., *Sens. Actuators B* 77, 116 (2001). © 2001, Elsevier.

conditions on SnO_2 sensor performance (e.g. [49–51]), there are relatively few studies that document the film microstructure. Figure 13 presents TEM images of typical sputtered SnO_2 thin films obtained by Horrillo et al. [52]. Note the columnar arrangements of the SnO_2 grains and the porosity of the films. Nagasawa et al. [53] also observed columnar microstructure for porous SnO_2 thin films, but not for dense SnO_2 thin films obtained at higher sputtering pressures.

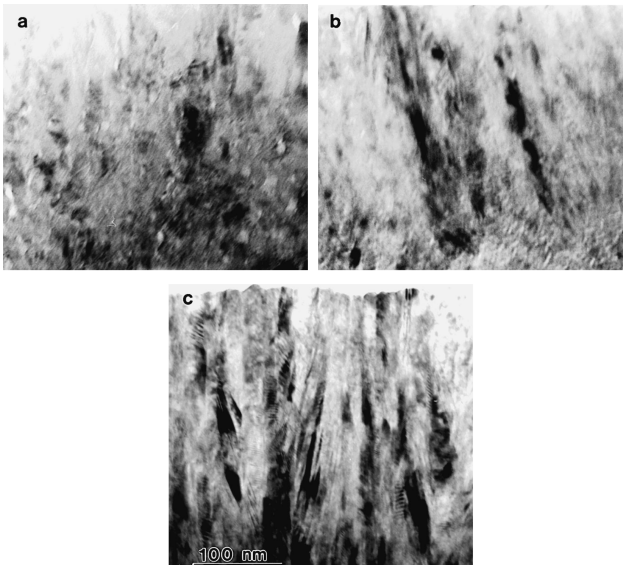

Figure 13. TEM images of tin oxide thin films (cross sectional images, no additives) generated by r.f. magnetron sputtering with deposition at (a) room temperature, film thickness ~200 nm; (b) 250 °C, film thickness ~200 nm; (c) 250 °C, film thickness ~400 nm. The size bar represents 100 nm. Reprinted with permission from [52], Horrillo et al., *Sens. Actuators B* 58, 474 (1999). © 1999, Elsevier.

Nicoletti et al. [54] used pulsed laser ablation to deposit a 380 nm SnO_2 layer onto a SiO_2 buffer layer on a Si substrate. As seen in the micrograph image shown in Figure 14, the grains exhibited a columnar growth formation with SnO_2 particle sizes between 20–60 nm, similar to the sputtered SnO_2 films. The films made using pulsed laser ablation also indicate the presence of voids as found in sputtered films. The selected area diffraction pattern (shown as the insert in Fig. 14) showed that the SnO_2 particle grains were randomly oriented and that the material indexed to cassiterite (α-phase) tin dioxide.

Gas-phase condensation can also be used to directly fabricate SnO_2 films [55, 56]. Kennedy et al. [56] used gas-phase condensation of SnO to produce tin dioxide thin films composed of virtually monodisperse SnO_2 particles. The authors also demonstrated good control of the average particle size (between 10 and 35 nm). The film morphology in general and specifically the average particle size showed good resistance to changes upon annealing. Figure 15 shows SEM images of the as-deposited film and the film after annealing at 300 °C for 1000 hours in O_2 and C_2H_5OH. Before annealing the film exhibited regular grain sizes, uniform deposition, good connectivity and a porous structure. After annealing, no significant variation in the morphology or average particle size was observed (the average particle size was verified via XRD analysis). The good stability of the films was attributed to the high-temperatures encountered by the SnO_2 particles during fabrication of the films.

As noted in the review by Göpel and Schierbaum [6], thin film tin oxide sensors offer considerable promise to overcome existing challenges of sensor design and performance. Indeed, much of the recent research and development of SnO_2 sensors focuses on thin film technologies. However, there is a clear need for additional studies investigating the effects of the final film microstructure, regardless of the synthesis method used (either direct film deposition or indirect). It is difficult to bridge the gap between atomistic models which represent interparticle connections between two nanosized SnO_2 particles, such as those discussed in Section 1, and overall sensor performance without these data.

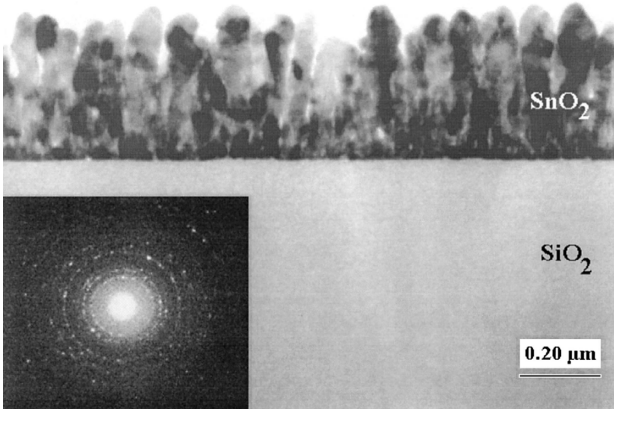

Figure 14. SEM image of tin oxide thin film (no additives) deposited on a SiO_2 layer using pulsed laser ablation. The corresponding selected-area diffraction pattern is shown as an insert in the Figure. Reprinted with permission from [54], Nicoletti et al., *Sens. Actuators B* 60, 90 (1999). © 1999, Elsevier.

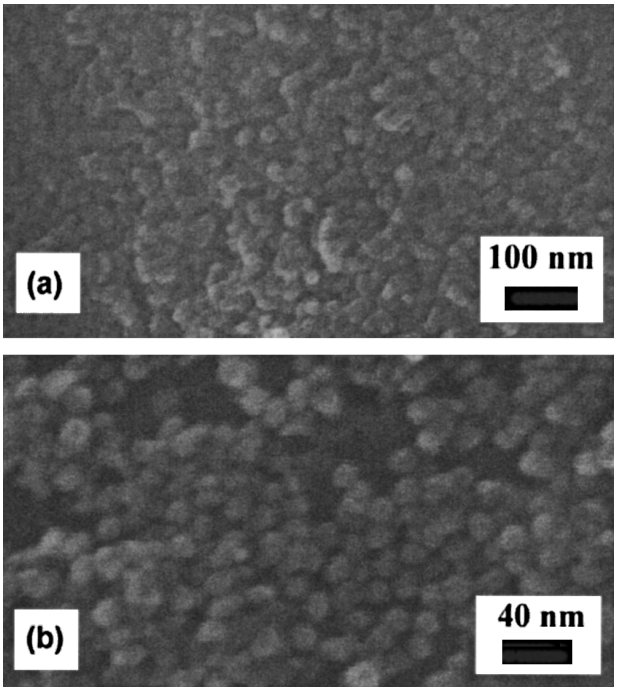

Figure 15. SEM image of as-deposited SnO_2 film (no additives) generated using gas-phase condensation of SnO (top) and film after 1000 h of annealing at 300 °C in O_2 and C_2H_5OH (bottom). Reprinted with permission from [56], Kennedy et al., *J. Appl. Phys.* 93, 551 (2003). © 2003, AIP.

As noted earlier, most of the methods used for manufacture of pure tin oxide materials are relatively competitive with respect to size of the SnO_2 particles produced, and post-synthesis processing can often dominate the final size of the SnO_2 crystallites in the gas sensor. Consequently, considerable efforts have been spent examining alternatives to reducing SnO_2 crystallite size for improving sensor performance, such as the use of dopants or additives, which are discussed in the following section.

2.2. SnO_2 with Additives

Tin oxide sensors show a dramatic improvement in sensitivity when the SnO_2 crystallites have particle diameters of 6 nm or less (see Figs. 1 and 2). The 2–6 nm size range is at the lower limit of the capabilities of the synthesis methods listed in Table 1, especially as the SnO_2 crystallite sizes can grow as the sensor is heat-treated (e.g. to obtain the necessary mechanical strength for the sensor). Therefore, alternative methods are required to improve sensor performance and recover the effects achieved by decreasing the particle size. Dopants or the use of additives can yield even more remarkable improvements in SnO_2 sensor performance as seen in the data of Figure 6, and as documented by many researchers (see [2, 6, 7, 9, 8] and references therein). All of the SnO_2 fabrication techniques discussed above have the capability to include additives in some form.

Important characteristics of some representative methods demonstrated for synthesis of doped SnO_2 are provided in Table 2. The reactant precursors used for the tin oxide and the additives, additive loadings, average SnO_2 crystallite size

Table 2. Representative synthesis methods, material characteristics and corresponding sensor sensitivity (where available) for SnO_2 systems with additives.

Doped SnO_2 synthesis method	SnO_2 precursor	Additive	Additive precursor	Additive loading (atomic ratio or % basis)	Form of SnO_2 produced	SnO_2 crystallite size	Demonstrated gas sensing performance	Sensitivity (Resistance ratio, R_a/R_g, at specified operating temperature and mole fraction of target gas)	Ref.
Sol–gel processing	$SnCl_4$	Ni, Os, Pd, Pt	$Pd(OOCH_3)_2$, $OsCl_3$, $PtCl_2$, $NiCl_2$	Metal:Sn 0.05:1	Film	4–12 nm	CO, NO_2, CH_4, C_2H_5OH, CH_3OH	• 7.0 (current measurements, I_g/I_a) at 250 °C, 1000 ppm of CH_4	[16]
	$SnCl_4$	CuO	Copper nitrate	Up to 50%, mole basis	Powder	20 nm	NO, CO_2, O_2	• 4.3 at 200 °C, 1000 ppm of NO	[13]
	$SnCl_4$	Pd, Pt, Au	$PdCl_2$, $PtCl_4$, $AuCl_3$	0.2% and 2%, weight basis	Powder	5–60 nm	CO, CH_4	• 8 at 400 °C, 500 ppm of CH_4	[17]
	Tin(II)2-ethylexanoate	Mo	Ammonium heptamolybdate	Mo:Sn 1:99 Mo:Sn 5:95	Powder	10–40 nm	CO, NO_2	• 2.4 at 350 °C, 100 ppm of CO	[59]
Sputtering	SnO_2	Pt, In, Al	Metal targets	N/A	Film	N/A	CO, NO_x,	N/A	[15]
	SnO_2	Au	Metal targets	N/A	Film	N/A	H_2	• 8 at 327 °C, 1000 ppm of H_2	[65]
Combustion synthesis	$SnCl_4$ in propane 1,2 diol	Sb	$SbCl_5$	1% and 5%, mole basis	Film	20–40 nm	C_2H_5OH	• 1.6 at 200 °C, 3200 ppm of C_2H_5OH	[60]
	$Sn(CH_3)_4$	Au, Pd, CuO/Cu_2O	$Au(O_2CCH_3)_3$, Au, Pd, $Cu(O_2CCH_3)_2$	Au ~3%, weight basis	Powder	8–20 nm	N/A	N/A	[66]
Pulsed laser ablation	SnO_2	Pt, Pd, Au	Metal targets	N/A	Film	20–60 nm	C_6H_6, CO, $C_6H_6 + CO$	• 1.2 at 400 °C, 30 ppm of CO[a]	[54]
Co-precipitation	$SnCl_4$	Au, Au + Pd	$HAuCl_4 \cdot 3H_2O$	0.1-10% Au, weight basis; 3% Pd, weight basis	Powder	2.5–21 nm	CH_4, CO, CO_2, C_3H_8, C_4H_{10}	• 0.8 at 400 °C, 3000 ppm of CH_4	[62]

[a]Sensitivity given as a conductance measurement, where $S = (G - G_o)/G_o$.

and sensor performance data (where available) are provided in the table. Note the average size of the tin oxide particles for doped materials is in the same size range as that for undoped SnO_2, and the additive loadings required for improved sensor performance are low (typically less than 10% mass or mole basis).

As discussed earlier, additives can have several effects on the SnO_2 properties important to gas sensing applications, including inhibiting SnO_2 grain growth, modifying the electron Debye length and modifying the gas-surface interactions via the electronic and catalytic mechanisms. Figure 16 shows the effects of Pd, Pt, and Au addition on SnO_2 crystallite size distribution for sol–gel generated SnO_2 as determined by Cabot et al. [17]. The average SnO_2 particle sizes for the three mixtures studied (as determined from the TEM images shown in Fig. 16) were 34 nm, 20 nm, and 26 nm for Au, Pd, and Pt, respectively. Thus, each additive affects the SnO_2 particles to a different degree and possibly via different mechanisms. Siciliano [16] also found average SnO_2 particle dimensions varied for Pd, Pt, Os and Ni additives compared to undoped SnO_2. Cabot and co-workers [17] suggested that two mechanisms can be at work in affecting the SnO_2 crystallite size. The additives can block SnO_2 particle growth and/or affect the rate of formation of crystallographic defects in the SnO_2 nanoparticles.

Cabot et al. further [17] explored the effects of additives on tin oxide particle growth during calcination. Figure 17 shows the average SnO_2 crystallite size determined via XRD analysis at various stages of an 8-hour, heat-treatment process. During the calcination process, the authors found the doped SnO_2 particles could grow from an initial size of about 7 nm to as large as 40 nm, as seen in Figure 17. The effect of additive loading is also shown in Figure 17. Increased palladium and platinum loadings systematically led to smaller SnO_2 crystallite sizes for calcination temperatures greater than 400 °C. However, except for calcination temperatures over 900 °C, the gold loading did not change the SnO_2 particle size. Based on the results of Figures 16–17, the authors concluded that the additives alter the kinetics of SnO_2 particle coalescence.

Distinguishing between the role of additives on modifying the SnO_2 electronic properties (e.g. altering the Debye length) and the role of additives on modifying gas-surface

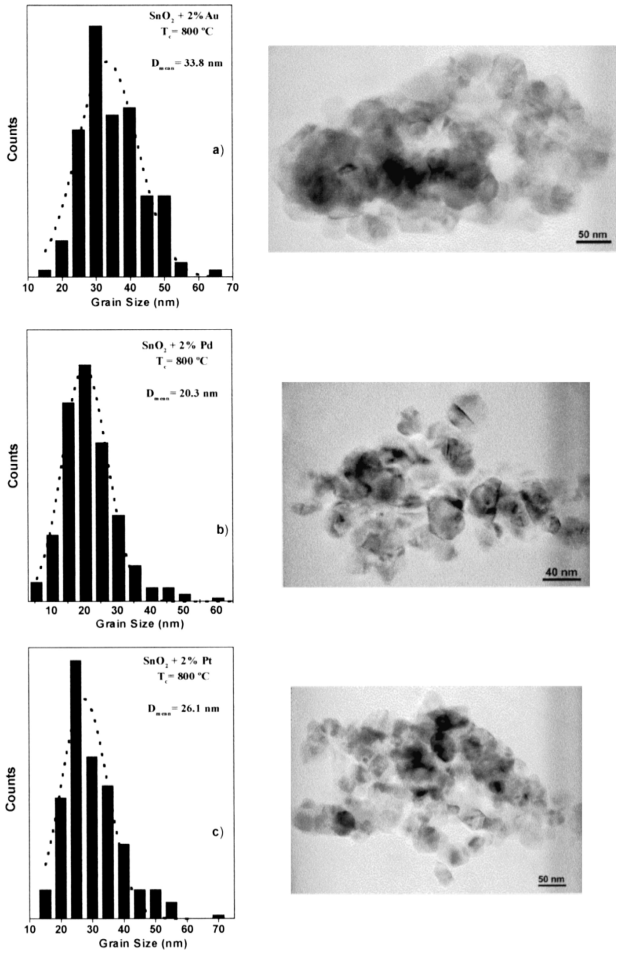

Figure 16. The effect of Au, Pd and Pt additives on tin oxide particle size distributions. The data and images from the top to bottom are from 2% Au-doped, 2% Pd-doped and 2% Pt-doped (mass basis) SnO_2 materials generated using sol–gel synthesis and calcined at 800 °C. The additives were introduced during the precipitation process and before thermal stabilization of the SnO_2. Reprinted with permission from [17], Cabot et al., *Sens. Actuators B* 70, 87 (2000). © 2000, Elsevier.

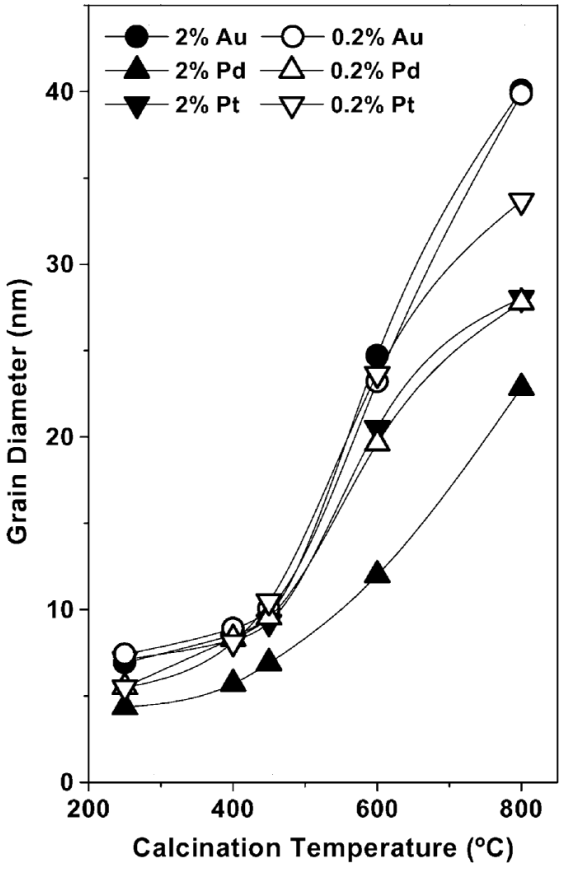

Figure 17. The evolution of the average SnO_2 particle size as a function of the processing temperature, type of additive and additive loading (mass basis loadings are provided in the legend). All materials were generated using sol–gel methods, and the additives were introduced during the precipitation process and before thermal stabilization of the SnO_2. Reprinted with permission from [24], Cabot et al., *Sens. Actuators B* 79, 98 (2001). © 2001, Elsevier.

interactions is much more difficult to do in comparison to quantifying the effects of additives on inhibiting SnO_2 particle growth. Primarily the challenge lies in identifying the morphology and location of the additives in the tin oxide and the chemical state of the additives. In general, the additives are present in multiple forms and it is not easy to quantify the relative impact of the forms of the additives. For example, TEM images of Au-doped combustion generated SnO_2 are shown in Figure 18. The Au particles are clearly identifiable in the images as the high-contrast spherical particles (the gold composition was confirmed via TEM-EDS analysis). Figure 19 shows the corresponding Au-particle size distribution as determined from TEM imaging. Smaller clusters of gold atoms (less than 5 nm in size) may also be present on the tin oxide particles or gold atoms may be dispersed in the SnO_2 lattice structure. However, direct TEM imaging cannot reveal the presence of these smaller units of gold. Figure 20 presents TEM imaging from Cabot et al. [24], of Au-doped and Pt-doped sol–gel generated SnO_2 materials. Again, the Au particle is clearly identified in the image as a relatively large, high-contrast particle. Gatan Image Filtering (GIF) analysis supports the identification of the gold particle. In the work by Cabot et al. [17], the authors identified by XPS analysis that Au and Pt metal clusters were present on the surface of the SnO_2 nanoparticles. The Au clusters are not observed in the TEM or GIF imaging, presumably due to the low signal levels associated with the small cluster sizes. The authors proposed that it is the small clusters of surface gold that are responsible for the changes in the SnO_2 sensor performance, not the larger particles identifiable in the TEM images.

In studies of sol–gel generated, Pd-doped SnO_2, Yamazoe [7] found the palladium dispersed as small particles (5–10 nm) on the surface of the tin oxide crystallites. Labeau et al. [57] identified a similar structure of dispersed platinum nanoparticles in their study of Pt-doped SnO_2 films made using spray pyrolysis. Figure 21 presents a high resolution TEM image from the study by Labeau and co-workers [57]. Note that one effect of the Pt on the SnO_2 can be seen in the image as a distortion induced in the SnO_2 crystal structure at the platinum particle/tin oxide particle interface. Further complicating the identification of the location of the additives in doped-tin oxide systems,

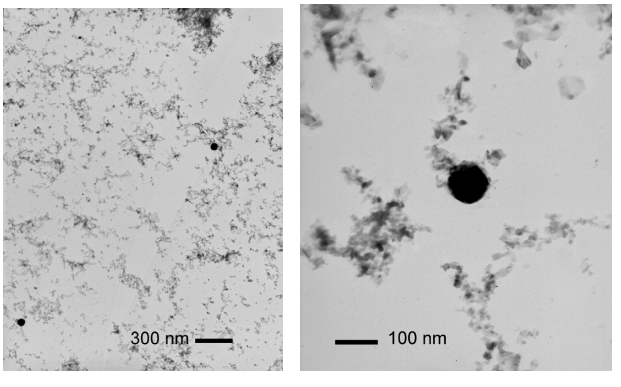

Figure 18. TEM images of combustion-generated, Au-doped SnO_2 powders. The high contrast spherical particles are gold, as identified using TEM/EDS. Synthesis details can be found in Miller et al. [66].

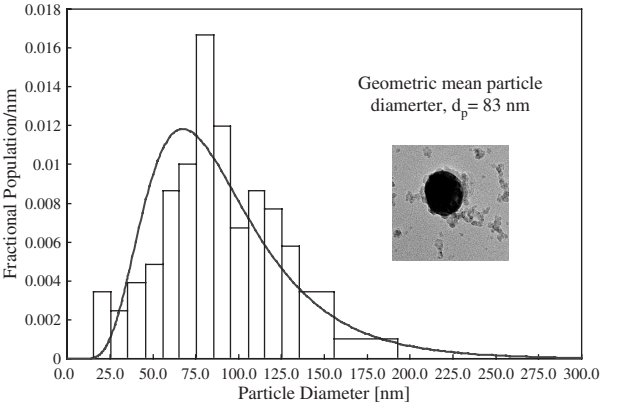

Figure 19. Size distribution of Au particles in Au-doped, combustion generated SnO_2 powders. The Au particle diameters were determined from TEM images, such as the insert shown in the Figure, and assuming spherical particle shapes. The solid line represents a log-normal size distribution.

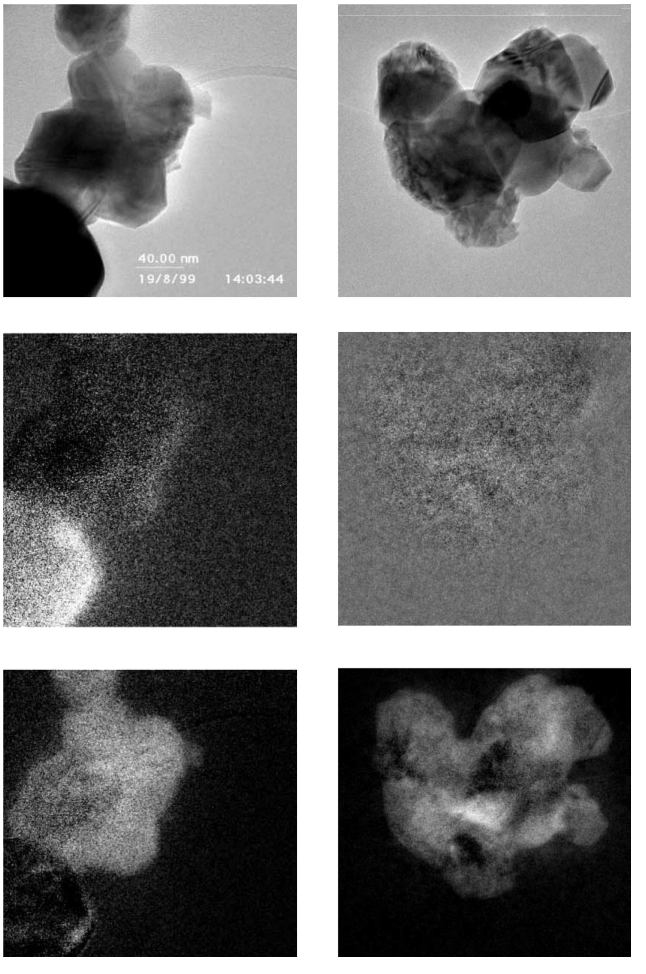

Figure 20. TEM micrographs of 2% Au-doped SnO_2 (left) and 2% Pt-doped SnO_2 (right). All materials were generated using sol–gel methods, and the additives were introduced in the precipitated SnO_2 solution. Loadings are provided on a mass basis. The middle panels are Au- (left) and Pt- (right) element maps (obtained by GIF analysis). The bottom panels are Sn-element maps (obtained by GIF analysis). The size bar represents 40 nm. Reprinted with permission from [24], Cabot et al., *Sens. Actuators B* 79, 98 (2001). © 2001, Elsevier.

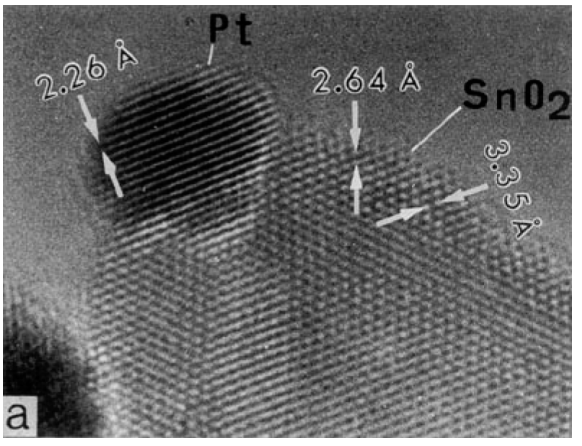

Figure 21. High resolution TEM image of 11% Pt-doped SnO_2 (mole basis) showing the distortion of the SnO_2 lattice near the Pt/SnO_2 interface. The doped SnO_2 films were made using spray pyrolysis. Reprinted with permission from [57], Labeau et al., *J. Solid State Chem.* 102, 434 (1993). © 1993, Academic Press, Inc.

Cabot et al. [24] found that the dopants could evaporate (as the authors observed for Pt) or migrate into the SnO_2 lattice structure (as the authors observed for Pd) during calcination. Montmeat et al. [23] documented similar mobility of additives. They found that gold deposited on the surface of a 20 μm thick SnO_2 film diffused throughout the film after heat treating at 700 °C for 15 hours. Thus, the location of the additives is a strong function of both the synthesis process used and the subsequent heat processing employed.

The chemical state or composition of the additive is also often unknown and can change as a function of the materials processing. For example, XRD spectra of Au-, Pd-, and Cu-doped, combustion-generated SnO_2 powders are shown in Figure 22. Note the tin oxides remain as crystalline cassiterite phase. Only pure metallic phases are identified in the gold and palladium systems, whereas only copper oxides are identified in the Cu-doped system. On the contrary, XRD analyses conducted by Cabot et al. [24] of sol–gel generated, Pd-doped SnO_2 yield metallic Pd-peaks only after significant high temperature calcination. As with the combustion-generated materials, the gold-doped sol–gel generated SnO_2 powders indicated only the metallic phase of Au. The combination of XPS, Raman and GIF analyses led Cabot et al. [17, 24] to conclude that at lower calcination temperatures, Pd was uniformly dispersed throughout the SnO_2 crystallites (see Fig. 20), and the Pd was in 2+ and 4+ states. They found similar results for platinum additives, and Figure 23 shows the results for the distribution of Pd and Pt chemical states as a function of the calcination temperature. The authors suggest in [17] that the 2+ states for Pd and Pt are linked to the SnO_2 structure, while the 4+ states are not. Thus, the 2+ chemical states are responsible for the effects on the SnO_2 sensing properties. Cabot et al. [17] also proposed that the chemical states may be localized in the SnO_2 nanoparticles (e.g. 4+ states near the surface of the SnO_2 crystallites, but not in the interior).

Other groups have demonstrated that the distribution of the additives throughout tin oxide film structures can

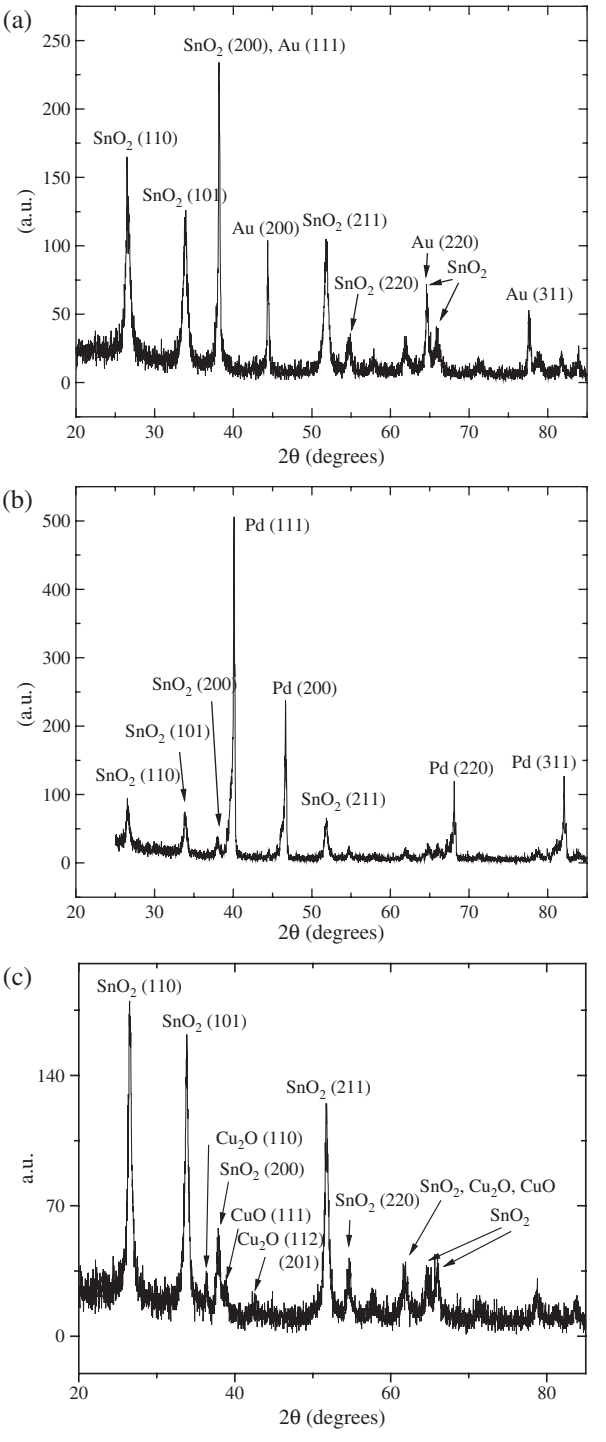

Figure 22. XRD spectra of (a) Au-, (b) Pd- and (c) Cu-doped, combustion-generated SnO_2 materials. Miller indices of the features attributed to the cassiterite phase of SnO_2 and the metal additives are indicated in the Figures. Synthesis details can be found in Miller et al. [66].

have significant impact on sensor performance. For example, Bittencourt et al. [70] studied the differences in sensor performance between a uniform distribution of Pt additives versus Pt additives localized near the surface of a thick film. The films were generated using printing technologies where the platinum precursor was mixed with the SnO_2

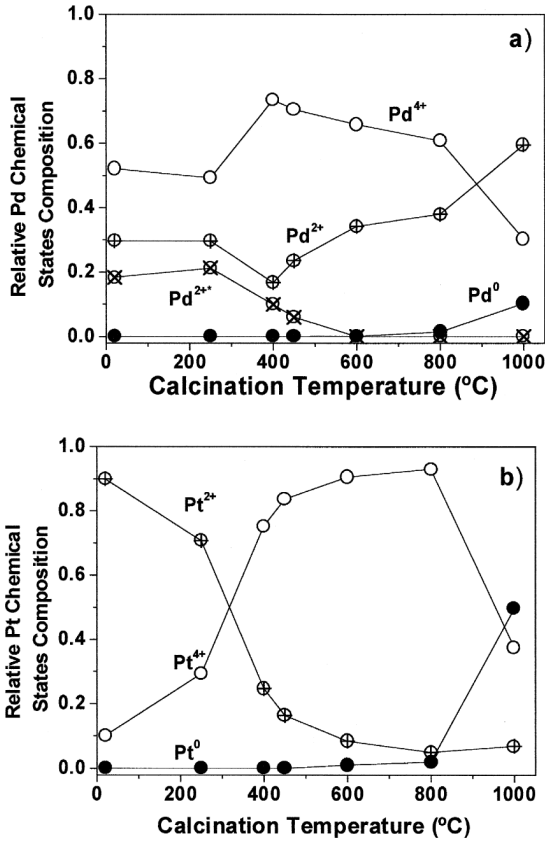

Figure 23. The distribution of chemical states of palladium (top panel) and platinum (bottom panel) as a function of calcination temperature in Pd- and Pt-doped (2% additive loadings, mass basis), sol–gel generated SnO_2. Reprinted with permission from [17], Cabot et al., *Sens. Actuators B* 70, 87 (2000). © 2000, Elsevier.

paste before printing to achieve the uniform dispersion, or the Pt additive was sputtered onto the surface of the SnO_2 film to achieve surface doping. Figure 24 presents SEM images of the two film structures which show the Pt-particle distributions in the films. Using XPS analysis, the authors identified 2+ and 4+ Pt states in both film structures, and the surface morphology (including crystallite size) of the SnO_2 appeared indistinguishable between the doped films samples. However, the sensors made with uniformly distributed Pt particles considerably outperformed the sputtered films (by approximately a factor of 4).

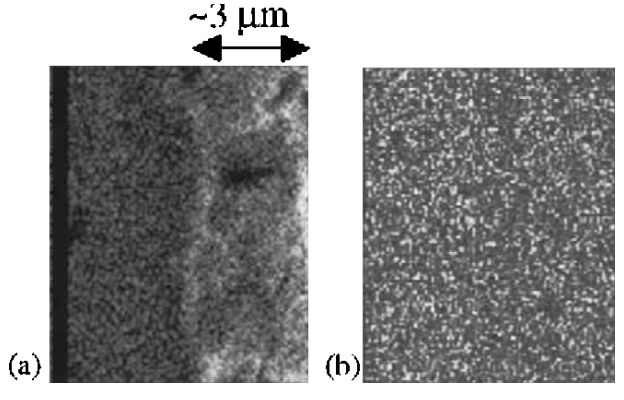

Figure 24. Cross sectional SEM images (back-scattered electron images) of Pt-doped SnO_2 thick films generated using printing of tin oxide pastes. The Pt additive was sputtered onto the surface of the SnO_2 film for the materials shown in (a) and the Pt additive was mixed with the SnO_2 paste (~3% Pt mass basis) before printing for the materials shown in (b). In the images, the bright areas correspond to Pt and the darker areas correspond to Sn. Reprinted with permission from [70], Bittencourt et al., *Sens. Actuators B* 97, 67 (2004). © 2004, Elsevier.

In a similar study of overall additive distribution, Chowdhuri et al. [47] examined the effects of organized distributions of copper additives on SnO_2 films. The authors compared performance of films where copper additives were deposited as CuO dots in an array across the surface of a SnO_2 film to SnO_2 films where a thin CuO layer was deposited onto the surface of the sensor. The films with the CuO-dot array displayed dramatically higher sensitivity (almost two orders of magnitude higher sensitivity to H_2S), than the SnO_2–CuO layered sensor. Unfortunately, the authors do not provide any microstructural or chemical state analyses of the SnO_2 or the Cu-additives for the two film systems. Thus, the work serves as an excellent example of both the considerable potential of tin oxide sensors and the difficulties associated with speculating what fundamental mechanisms are responsible for the enhancements without microstructural characterization data.

3. SENSOR PERFORMANCE

3.1. Sensor Types and Fabrication Methods

The types of SnO_2 sensors are distinguished by the characteristic dimensions of the active sensor material. For porous plug and sintered block sensors, the SnO_2 layer is generally on the order of a few millimeters in thickness, while the SnO_2 layer in film sensors is generally in the nanometer to micron range. Thin films span approximately 50 nm to 2 μm in film height, and thick films span approximately 2–10 μm. The sensor fabrication method varies according to the type of the sensor.

3.1.1. Porous Plug and Sintered Block Sensors

The simplest sensor design is a sintered block arrangement, an example of which is shown in Figure 25. The block is prepared by sintering tin oxide powder with the electrode wires embedded in the block. The operating temperature of the sensor is controlled by a heater incorporated with the sensing electrodes. Commercial units of sintered block sensors include a fine mesh (see the sensor housing schematic shown in Fig. 25) that prevents combustible gases from igniting at the high operating temperatures of the sensor.

The porous plug sensor arrangement is slightly more complex than the sintered block, as seen in the schematic shown in Figure 25. The porous plug sensor typically consists of a thin-walled ceramic tube with an internal diameter on the order of 1 mm. The electrodes are deposited on the external wall of the ceramic tube. A wire coiled inside the sensor is used to heat the system. The SnO_2 sensing material is sintered onto the external surface of the ceramic tube with a thickness of a few millimeters. As shown in Figure 25, the SnO_2 sensors are typically mounted in a housing where the test gases are directed onto the meshed entrance of unit.

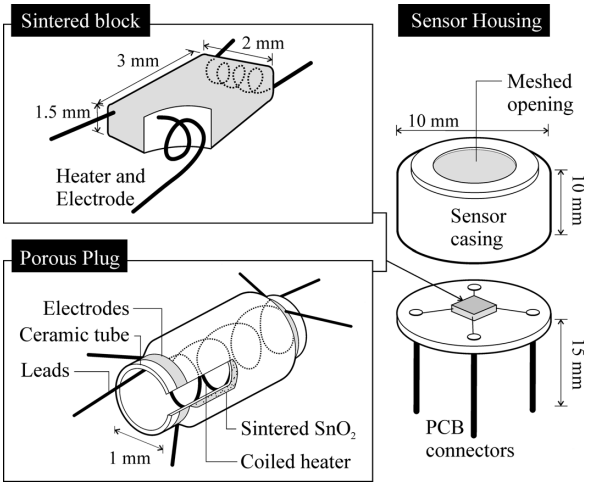

Figure 25. Schematics indicating sintered block sensor design (top left) and porous plug sensor design (bottom left) with sensor housing on the right. Typical dimensions are provided in the diagrams.

3.1.2. Thin and Thick Film Sensors

The general architecture of thick and thin SnO_2 films is very similar, and Figure 26 shows the typical components of tin oxide film sensors. Figure 27 is an SEM image of a thick film sensor which shows the clear transitions between the SnO_2 sensing material and the electrode materials. Both the thin and thick films incorporate a substrate (typically alumina) that contains the printed electrodes (typically platinum or gold). A heater is often integrated with the substrate design, as shown in Figure 26. For thick films, screen-printing technologies are quite widespread, while for thin films, sol gel deposition, spin-coating, and sputtering techniques are preferred. Thick and thin film SnO_2 sensors are generally favoured compared to sintered block and porous plug sensors due to the low power consumption and better sensor performance, such as time response.

Table 3 lists characteristics of some selected methods for fabrication of thick- and thin-film SnO_2 sensors. Between thin and thick films, current research tends to focus on thin films due to their superior sensor performance characteristics. The particular references in Table 3 were

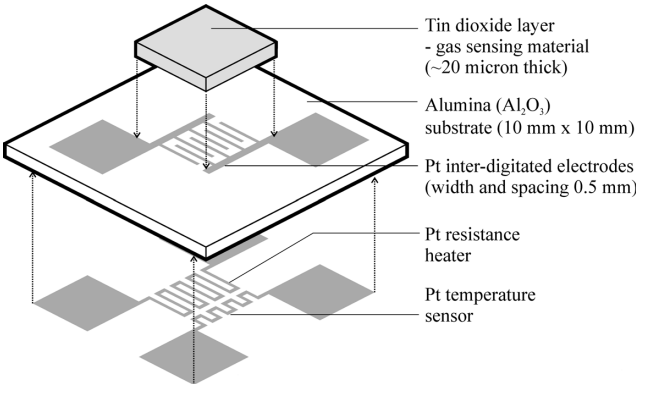

Figure 26. Schematic of typical sensor architecture used for thin or thick SnO_2 films. Dimensions provided in the schematic are representative of thick films.

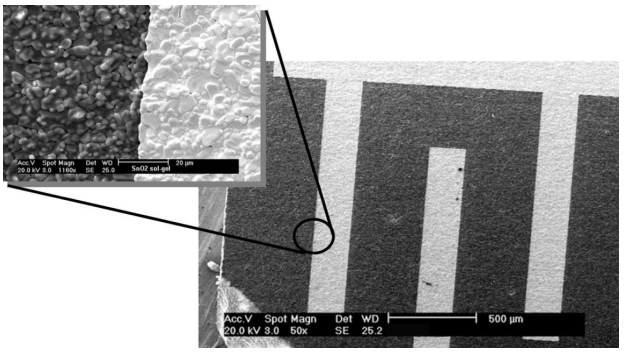

Figure 27. SEM image of the surface of an undoped-SnO_2 sensor and the configuration of the interdigitated electrodes. The films were created by spin coating sol–gel SnO_2 onto alumina substrates. Reprinted with permission from, Capone et al., *Sensors and Actuators B: Chemical* 77, 503 (2001). © 2001, Elsevier.

chosen based on the availability of sensor performance data for comparable gas-sensing systems (typically for detection of ethanol or methane). Sensor operating temperatures and mole fractions of target gas are provided in the table. Information is also provided on the sensor fabrication method and the synthesis method used to make the SnO_2.

As presented earlier in Section 2, critical steps in sensor fabrication often involve heat treating the SnO_2 sensing materials. For example, sintering involves heating the sensor at sufficiently high temperatures to cause the particles to fuse for increased connectivity and mechanical strength. As seen in Figure 17, heat treatments also tend increase the average SnO_2 particle size, and they can lead to migration and transformation of metal additives (e.g. see Fig. 23). Organic binders and silicates are often employed to prevent excess crystal growth and improve bonding. The temperature range for sintering is typically between 500–700 °C, and sintering times typically range between 30 minutes to 2 hours. As seen in Tables 1 and 2, many sensor fabrication methods may also involve a calcination step (where the sensing material is heated to approximately 450 °C) that is used to drive off the impurities (such as chlorine) that may be present in the SnO_2. Generally, the first studies conducted to benchmark a sensor design are investigations of the optimal sintering temperature in terms of sensor performance.

3.2. Sensitivity

As noted earlier, the sensitivity of the SnO_2 gas sensor is typically defined as the ratio of the resistance of the sensing element in air to that in the target gas, R_a/R_g, although conductance measurements are also used (see Table 3). For oxidizing gases such as H_2 and CO, the resistance in the target gas, R_g, is generally lower due to the oxygen desorption mechanism at the surface of the tin oxide sensor. The sensitivity is highly dependent on film porosity, film thickness, operating temperature, presence of additives and crystallite size.

Even though porosity is expected to have a large impact on sensor sensitivity, there have been few studies that quantify sensor porosity. Licznerski et al. [69] report average pore radius and BET specific surface areas for their investigation of rhodium-doped SnO_2 sensors. Such results facilitate

Table 3. SnO_2 film sensor synthesis methods and corresponding sensor performance.

Film type (film thickness)	Sensor fabrication method	SnO_2 synthesis method	SnO_2 crystallite size	SnO_2 additive	Sensor performance (sensitivity[a], selectivity and stability; where provided)	Time response	Ref.
Thick (N/A)	Screen printing	Wet method* (Co-precipitation)	9 nm	Au, Pd	• 0.6 at 400 °C, 1000 ppm of CH_4 • Qualitative selectivity data	N/A	[62]
Thick (20–25 μm)	Screen printing	Commercial powder	N/A	Pt	• 800 at 300 °C, 1000 ppm of C_2H_5OH • Selectivity number provided	8 s	[67]
Thick (20–25 μm)	RF magnetron sputtering	Commercial powder	N/A	Pt	• 100 at 300 °C, 1000 ppm C_2H_5OH[b]	12 s	[67]
Thick (20–25 μm)	DC-sputtering	Commercial powder	N/A	Ag, Ti	• 80 at 300 °C, 1000 ppm C_2H_5OH[b]	7–15 s	[67]
Thick (250 μm)	Screen printing	Commercial paste	N/A	Pd	• 3.5 at 470 °C, 1000 ppm of CH_4 • Qualitative selectivity data	N/A	[68]
Thick (N/A)	Screen printing	Commercial paste	30 nm	Rh	• 3.5 at 500 °C, 1% of CH_4	N/A	[69]
Thick (N/A)	Screen printing	Commercial paste	60 nm	Pt	• 800 at 300 °C, 1000 ppm of C_2H_5OH	15 s	[70]
Thin (1.5 μm)	Gas-phase condensation	Gas-phase oxidation (SnO precursor used)	14 nm	None	• 3.5 at 300 °C, 1000 ppm of C_2H_5OH	10 s	[56]
Thin (100 nm)	Spin-coating	Commercial colloidal dispersion	10 nm	None	• 0.08 $k\Omega^{-1}$at 350 °C, 1 ppm CH_3OH (sensor conductance) Stability shown for 120 h	N/A	[71]
Thin (1 μm)	Spin-coating	Wet gel*	6 nm	None	• 1100 at 350 °C, 800 ppm of CO	20 s	[34]
Thin (300 nm)	Spin-coating	Hydrothermal treatment*	6 nm	None	• 400 at 350 °C, 800 ppm of H_2	N/A	[72]
Thin (300 nm)	Spin-coating	Mechanochemical reaction*	24 nm	None	• 5 at 300 °C, 1000 ppm of O_2	120–180 s	[73]
Thin (500 nm)	Ion-beam sputtering	Precipitation*	11 nm	Ca	• 1.3 at 400 °C, 4000 ppm of CH_4 • Stability shown for 90 days	N/A	[45]
Thin (200 nm)	Reactive DC sputtering	N/A	12 nm	Pt, Pd	• 5.25, at 325 °C, 100 ppm of CO[b] • Stability shown for 75 days • Qualitative selectivity data	5 s	[46]
Thin (120 nm)	RF diode sputtering	Commercial tin target	N/A	CuO	• 7443 at 150 °C, 20 ppm of H_2S • Stability shown for 1000 s	14 s	[47]
Thin (380 nm)	Pulsed laser ablation	N/A	20–60 nm	Au, Pd, Pt	• 1.2 at 400 °C, 30 ppm of CO[b] • Stability shown for 200 h	10 s	[54]

*$SnCl_4$ used as the SnO_2 precursor.

[a]Sensitivity given as a resistance ratio, $S = R_a/R_g$, at specified operating temperature and mole fraction of target gas.

[b]Sensitivity given as a conductance measurement, where $S = (G–G_o)/G_o$ at specified operating temperature, when exposed to mole fraction of target gas.

better comparison of sensor fabrication techniques and their performance.

In the following paragraphs, the effects of SnO_2 crystallite size, operating temperature, and additives on SnO_2 sensor sensitivity are presented using representative results whose performance measurements have been tabulated in Table 3. The most significant parameter affecting sensor sensitivity is the average SnO_2 particle size. As seen in Figures 1 and 2, the work performed by Yamazoe et al. [7] shows that decreasing crystallite size leads to an increase in sensitivity by orders of magnitude for sizes below 7–9 nm. Also note from their results that beyond crystallite sizes of 50 nm the effect of particle size is significantly diminished. As discussed earlier, such results drive tin oxide sensor research towards fabricating SnO_2 sensors that have grain sizes below 7–9 nm; however, there are considerable challenges with achieving and retaining these small dimensions for practical gas sensors.

Another significant parameter affecting tin oxide gas-sensor sensitivity, that is a more controllable optimization variable, is the sensor operating temperature. Optimization of the operating temperature is crucial for establishing high sensitivity of the SnO_2 sensor to the target gas. For example, Figure 28 presents the results by Cavicchi et al. [71] on the effects of sensor operating temperature on the performance of a thin-film SnO_2 sensor used for detection of methanol. Their results substantiate that there is an optimum operating temperature for the sensor, where the sensitivity to the target gas is the highest. Similarly, the results of Min and Choi [45] for undoped-SnO_2 thin film sensors, shown in Figure 29, show very clearly the dependence of sensitivity on operating temperature. A maximum in sensitivity is observed at an operating temperature of about 400 °C in the work by Min and Choi. The peak can be explained as follows. At low temperatures there is less oxygen coverage, when

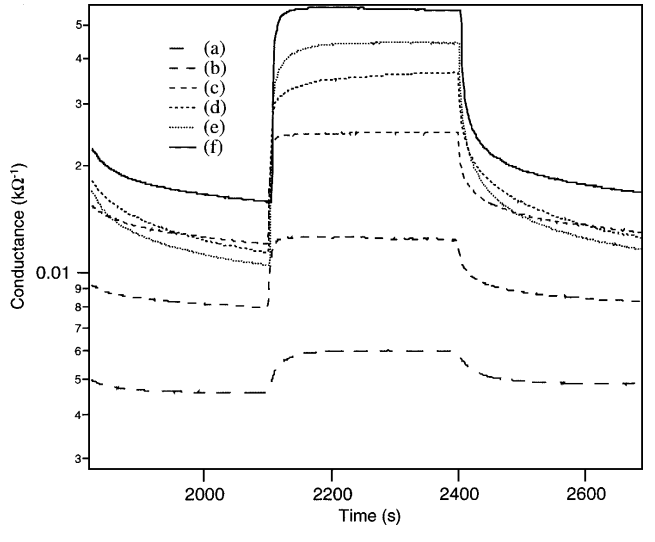

Figure 28. Doped tin oxide thin-film (100 nm thickness) response to methanol in dry air at 80 nmole/mole (80 ppb) at different sensor operating temperatures: (a) 150 °C (b) 200 °C (c) 250 °C (d) 300 °C, and (f) 400 °C. The films were generated by spin-coating Sb-doped commercial SnO_2 (15% additive loading) onto a substrate. Reprinted with permission from [71], Cavicchi et al., *Sens. Actuators, B: Chemical* 77, 145 (2001). © 2001, Elsevier.

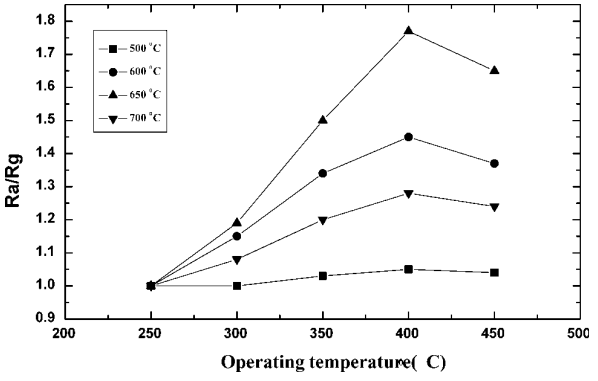

Figure 29. Sensitivity of undoped-SnO_2 sensors to various annealing temperatures (500–700 °C) as a function of the sensor operating temperature (for a target gas of 5000 ppm CH_4). SnO_2 thin films generated using ion beam deposition. Reprinted with permission from [45], Min and Choi, *Sens. Actuators, B: Chemical* 98, 239 (2003). © 2003, Elsevier.

the sensor is exposed to air and therefore when the target gases are introduced there is negligible change in sensitivity. As the operating temperature increases, the conductance response of the sensor increases due to the increasing rate at which oxygen is adsorbed; however, the desorption rate of adsorbed gases also increases with increasing temperatures. The decrease in sensitivity for temperatures above a critical operating temperature, T_{crit}, can be attributed to the higher desorption rates at these temperatures. When the target gases are introduced, the added desorption due to the target gases is small relative to the steady-state desorption in air, leading to a decreasing impact on the sensor response for $T > T_{crit}$. Due to the competing rates of adsorption and desorption, tin oxide sensors always tend to exhibit a maximum sensitivity at a particular operating temperature, which defines T_{crit}. Generally the operating temperature of the sensor is set as close to T_{crit} as possible in order to achieve maximum sensitivity. Note that T_{crit} may vary for the same sensor when exposed to different target gases, a fact that can be utilized to improve selectivity which is discussed below.

As presented earlier, introduction of dopants into the SnO_2 sensing materials can also improve sensor performance. Several mechanisms have been proposed to explain the observed behaviour. Two mechanisms (the electronic and chemical mechanisms which were discussed in Section 1) have been generally well accepted. Chowdhuri and co-workers [47] describe the chemical mechanism as a spill-over effect, where there is an increase in surface concentration of adsorbed gases. They describe the electronic mechanism as a Fermi-level energy-control effect which gives rise to a high surface barrier at the intergranular contacts. Motivated by enhancing the chemical effect, noble metal catalysts Pt, Pd, Ag, Rh, Au, and Ir are often used as additives in SnO_2 sensors. The effects of these additives can be quite remarkable on SnO_2 sensor sensitivity. There are numerous examples of the effects of additives on tin oxide sensitivity in the literature (see [4, 7–9], and references therein). To provide some perspective for the enhancements that can be achieved, Figure 30 presents results from Ivanov et al. [67] for thick Pt-doped SnO_2 films used to detect ethanol vapor. For comparison purposes, the sensor response of an undoped SnO_2 sensor is provided in

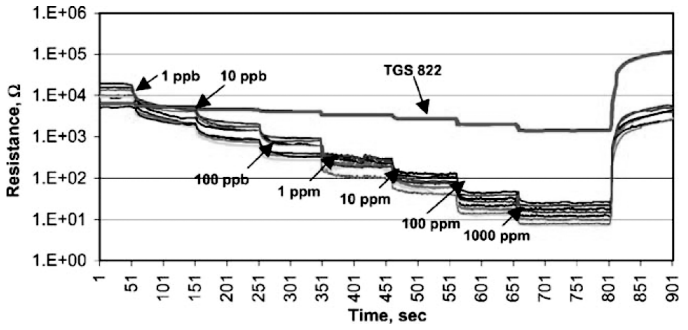

Figure 30. Response of the eight thick-film Pt-doped SnO_2 sensors operating at 300 °C to successive injections of ethanol. The films were generated using paste/screen printing methods with commercial SnO_2 powder and ~1.7% Pt loading (mass basis). Reprinted with permission from [67], Ivanov et al., *Sens. Actuators, B: Chemical* 99, 201 (2004). © 2004, Elsevier.

the Figure. A substantial increase in sensitivity was observed in the Pt-SnO_2 materials compared to the commercially available undoped SnO_2 counterpart (labelled TGS 822). In Figure 30, the various Pt-SnO_2 response curves also indicate the high degree of repeatability of the performance of the Pt-SnO_2 sensors, which were each manufactured using the same method.

As expected, the SnO_2 sensor sensitivity is a function of the loading and the morphology of the additive. For example Figure 31 presents the results of Sung et al. [62], who found dramatic improvements in the sensitivity performance of a thick-film methane sensor by optimizing the amount of gold particles in the sensing material. By controlling the addition of gold particles, the sensitivity to methane almost doubled. The authors attributed their results to achieving SnO_2 crystallite sizes that were comparable to the theoretical value for optimum particle size for the 1% Au case (based on the electron Debye length according to the equation $2L_D = 0.8$ d_p, where L_D is the Debye length and d_p is the SnO_2 particle size). The results suggest that gold acts to control the SnO_2 particle size rather than as a catalyst in this system.

The effects of additives on sensor performance are complex and it is not always easy to assess what role the additives are playing on the chemical and physical mechanisms important in SnO_2 gas sensors, and it should be noted that dopants do not always enhance sensor performance. Figure 32 is an example, where Choi and co-workers were trying to control the crystallite growth by introducing a growth inhibitor (Ca) [45]. The additive decreased the SnO_2 crystallite size, which should have enhanced the sensor sensitivity. However, in the circumstances studied, the Ca reduced the sensor sensitivity and further indicated instability in the long-term sensitivity response of the sensor. Min and Choi [45] suggest that the surface roughness was the cause for the anomalous results. Clearly, careful examination of the microstructural and electronic properties of doped-SnO_2 systems is vital towards understanding the performance of these nanocomposite systems.

3.3. Selectivity

Selectivity relates to the specificity of the gas sensor response to a target gas in the presence of a mixture of gases. Selectivity plays a major role in gas identification. Generally, a 'fingerprinting' method relies on a unique signature of the target gas signal. However, gases often produce very similar SnO_2 sensor responses (except when comparing reducing to oxidizing gases). For example, gases such as ethanol, carbon monoxide and methane have appreciable cross-sensitivity that hinders the development of a domestic gas sensor which can distinguish these species [46].

Common techniques of improving the selectivity of gas sensors include controlling the sensor operating temperature, selective gas filters used in series with the gas sampling and using additives. Different operating temperatures allow the control of the sensitivity towards a particular gas when there is a unique T_{crit} for each gas; thus allowing the sensor to produce distinguishable signals for two gases at a selected temperature. The film morphology and sensor architecture

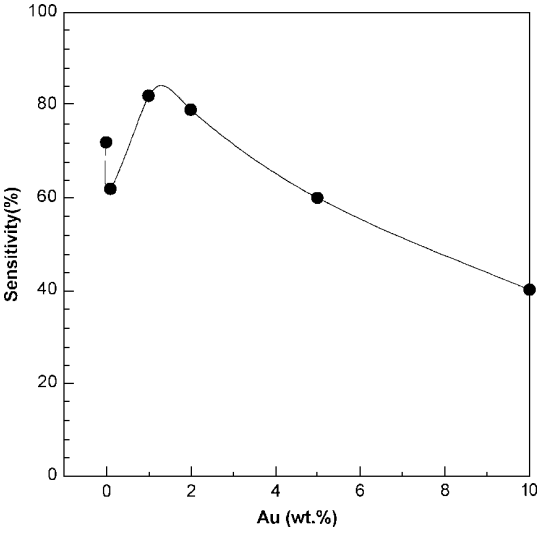

Figure 31. Tin-oxide sensor sensitivity as a function of Au loading (response to 3000 ppm CH_4 at an operating temperature of 400 °C, thick-film sensor generated using sol–gel processing). Reprinted with permission from [62], Sung et al., *Sens. Actuators, B: Chemical* 66, 149 (2000). © 2000, Elsevier.

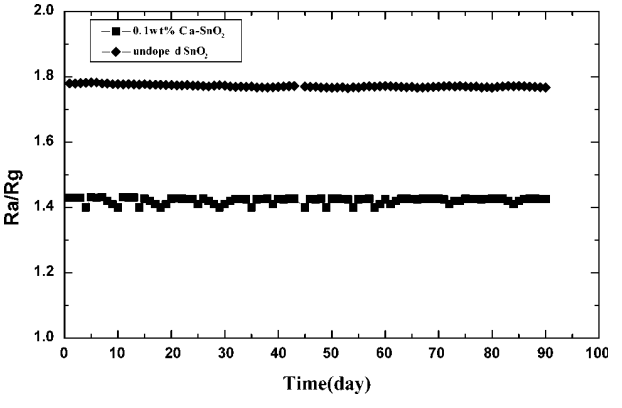

Figure 32. Sensitivity and long-term stability of undoped and 0.1 wt.% Ca-doped thin-film SnO_2 sensors. Sensors operating at a nominal temperature of 400 °C, 5000 ppm CH_4. The films were generated using ion beam sputtering. Reprinted with permission from [45], Min and Choi, *Sens. Actuators, B: Chemical*, 98, 239 (2003). © 2003, Elsevier.

can also play a key role in selectivity as indicated by Akbar et al. [9]. Distinguishing poorly-reactive gases from reactive gases can be facilitated by placing electrodes further inside the bulk of the sensing material to allow reactive materials to be filtered by the sensing material near the surface of the sensor. Another technique uses catalysts, which generally reduce the operating temperature of gas sensor for a particular gas species and thus allow the target gas to be distinguished from other gases due to the differences in sensitivity. In other words, addition of catalysts can maximize the sensitivity of target gases to produce a distinct signal.

In recent work, Heilig and co-workers [58] have proposed a novel means to improve SnO_2 sensor selectivity based on monitoring the sensor operating temperature. When the target gas interacts with the SnO_2 sensor, the reaction can be either endo- or exothermic, leading to a measurable change in the sensor operating temperature, ΔT_s, and the sensor resistance (i.e. the sensor sensitivity). Heilig et al. [58] demonstrated how the change in the sensor temperature and selectivity could be correlated to specific gases. Some of their results for ΔT_s, and R_a/R_g for sequential injection of target gases are shown in Figure 33. Using calibration curves such as those shown in Figure 34, the authors were able to use sensor response data like those of Figure 33 to uniquely identify each target gas. Takada and co-workers have explored the potential of using changes in the sensor temperature, resistance, capacitance, and inductance for improved gas monitoring [68], and references therein, and they have confirmed the method of simultaneous monitoring of ΔT_s, and R_a/R_g as a powerful technique that allows one sensor to be used to both discriminate between gases and quantify the amount of target gas present. One limitation of this method is in the application of detection of a target gas in a mixture which may contain significant levels of interference gas species, e.g. detection of CO in a gas mixture which includes high levels of CO, CH_4 and C_2H_5OH. Multiple calibration curves would have to be generated for each mixture and uniqueness of the sensor response may become a concern.

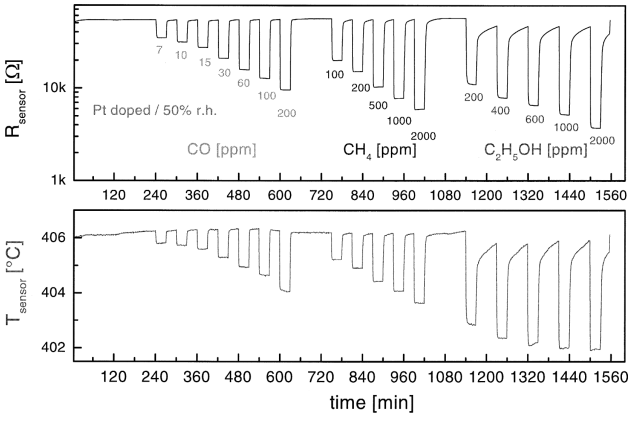

Figure 33. Typical response of a Pt-doped thick film SnO_2 sensor (0.2% additive loading, mass basis, thick-film sensor generated by deposition of doped-SnO_2 suspensions) upon sequential exposure to three target gases. Variation in sensor operating temperature provided in the lower panel. Reprinted with permission from [58], Heilig et al., *Sens. Actuators, B: Chemical* 58, 302 (1999). © 1999, Elsevier.

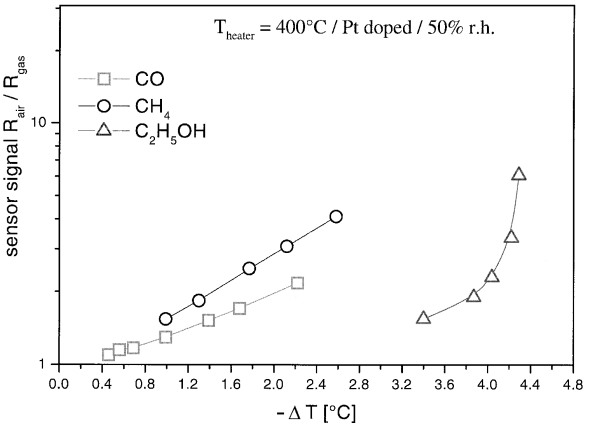

Figure 34. Demonstration of SnO_2 sensor selectivity by simultaneously monitoring the change in the sensor temperature and resistance upon exposure to different gases. Pt-doped SnO_2 thick film sensor operating at a nominal temperature of 400 °C (0.2% additive loading, mass basis, thick-film sensor generated by deposition of doped-SnO_2 suspensions). Reprinted with permission from [58], Heilig et al., *Sens. Actuators, B: Chemical* 58, 302 (1999). © 1999, Elsevier.

3.4. Stability

Stability is often given limited attention in tin oxide sensor development studies although it is a key quality indicator for gas detection. There are numerous studies in the literature on improving sensitivity and selectivity, but few studies supply stability data. The success of a sensor will be limited if the sensor performance is not demonstrated as repeatable and stable over long-term testing.

Problems of stability, as outlined by Park and Akbar [9], may be attributed to three primary areas of concern. The first is that a surface conductive sensor can suffer from surface contamination. Second, changes in the sensor characteristics (such as intergranular connectivity) can occur due to thermal expansion coefficient mismatch and/or interfacial reactions at the metal electrode/ceramic interface. Lastly, the film morphology may change over time due to the relatively high operating temperatures of the sensor, which may also cause migration of additives.

Figure 35 presents the results of Mandayo et al. [46] who studied the effects of platinum and palladium catalysts sputtered at various depths in a SnO_2 film. They discovered that a palladium layer at the bottom of the sensing material produced the greatest response and showed stability over a period of 75 days for the three gases investigated. The researchers pointed out that it is critical to allow the sensors to stabilize before they are put to service or the sensors would not function accurately.

3.5. Time Response

Generally, each of the sensor performance criteria is interdependent (e.g. sensitivity and selectivity). It is difficult to change one and not influence another key sensor property as seen in some of the previous examples. Time response is especially dependent on the sensor characteristics such as SnO_2 crystallite size, additives, etc.; and further consideration of electrode geometry, electrode position, diffusion rates, etc. need to be considered in order to reproduce or

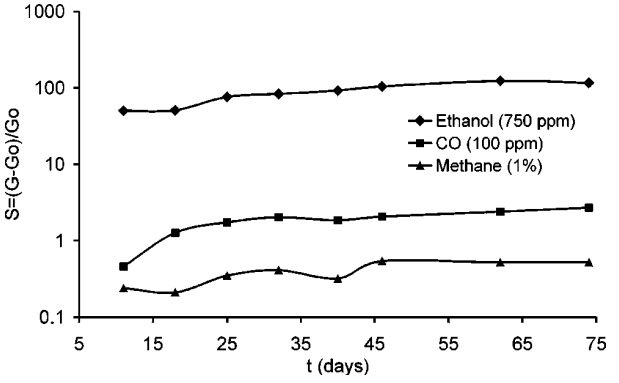

Figure 35. Long-term stability of Pt-doped tin oxide thin-film sensor response to three gases (Pt layer buried in sensor, operating temperature of 300 °C and 40% relative humidity, sensor fabricated using DC sputtering). Reprinted with permission from [46], Mandayo et al., *Sens. Actuators, B: Chemical* 95, 90 (2003). © 2003, Elsevier.

compare data from one sensor to another. For example, Figure 36 presents the work of Kennedy et al. [56] who have developed a unique synthesis and fabrication technique to control the SnO_2 crystallite size without changing the film thickness. The results for sensor sensitivity to ethanol as a function of time for three characteristic tin oxide particle sizes are presented in the Figure. The data clearly indicate a decrease in response time with a decrease in average SnO_2 particle size.

Chowdhuri and co-workers also demonstrated a unique method to improve sensor time response. Figure 37 shows the sensitivity of a SnO_2 sensor fabricated by Chowdhuri et al. [47] using a sputtering technique for pure SnO_2, CuO layered SnO_2 and CuO-dotted SnO_2 sensor architectures. They found a dramatic improvement in sensor time-response through addition of the copper additives and by controlling the catalyst structure to form an organized array of islands on the surface of the sensor. This work demonstrates the potential for micro-engineered architectures to even further enhance the beneficial properties of metal additives on SnO_2 gas sensors.

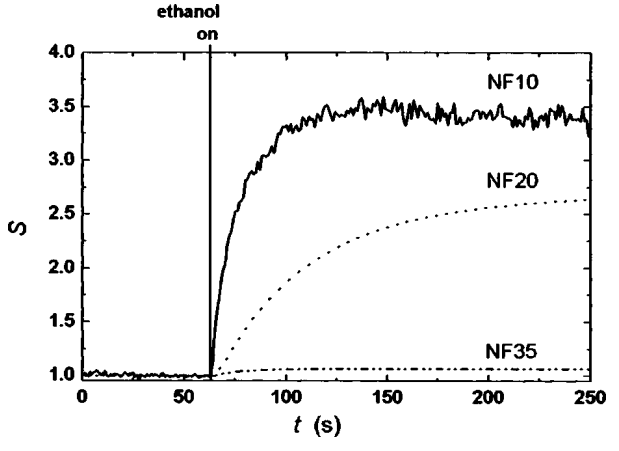

Figure 36. Dependence of tin oxide sensor transient response on SnO_2 particle size (operating temperature of 300 °C, 1000 ppm C_2H_5OH). Undoped-SnO_2 thin film sensors fabricated using gas-phase condensation. NF10 contains 10 nm particles, NF20 contains 20 nm particles and NF35 contains 35 nm particles. Reproduced with permission from [56], Kennedy et al., *J. Appl. Phys.* 93, 551 (2003). © 2003, American Institute of Physics.

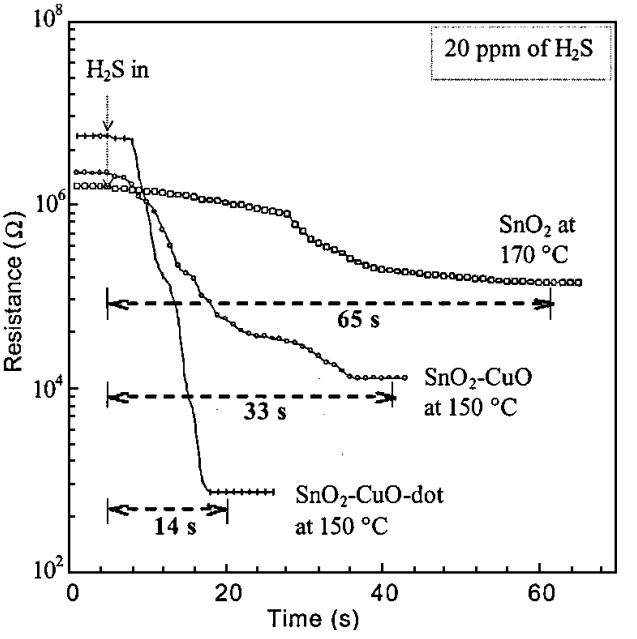

Figure 37. Comparison of the effect of CuO additives (10 nm CuO film and ~600 μm diameter CuO dots) on response time for thin-film SnO_2 sensors generated using reactive sputtering onto glass substrates. Operating temperatures are provided in the FIG.. Reprinted from Chowdhuri, Gupta and Sreenivas, *IEEE Sens. J.*, **3-6**, 680-686, Copyright IEEE (2003).

4. CONCLUDING REMARKS

The amount of progress demonstrated in the past 10 years towards expanding the capabilities and quality of SnO_2 sensors is remarkable. This work attempts to document some of the developments with a focus on the studies which explore the microstructural features of SnO_2 sensor materials and recent advances in enhancing sensor performance parameters. Many of the studies remain empirical in nature, as the basic principles underlying SnO_2 sensor performance continue to be a complex topic that spans orders of magnitude in spatial dimensions and includes heterogeneous physical and chemical phenomena.

Additives provide flexibility and potential to apply SnO_2 sensors to new gases, conditions, and systems. However, the effect of additives on sensor performance is dependent on the synthesis method and heat treatments used during sensor fabrication. Although there have been some extraordinary efforts to quantify and establish links between microstructure of doped-SnO_2 and the resulting sensor performance, there remains a need for better understanding of the fundamental mechanisms important in SnO_2 systems with additives. Specifically, development of more sensitive characterization tools (possibly electron-microscope based) which can be used to characterize the location, state and form of the additives in the SnO_2 are essential. TEM imaging can identify discrete additive particles (~2 nm and larger), but TEM cannot be used to image additives when

they are dispersed within the SnO_2 crystallites. High resolution TEM imaging can capture dislocations in the lattice of individual SnO_2 particles induced by the presence of additives in the particle, but the data are difficult to make statistically meaningful. X-ray diffraction techniques can provide statistically significant compositional data, but only if additives are present at sufficiently high concentrations that detectible XRD peaks are observed. Raman spectroscopy is a powerful and underutilized tool when combined with other analytical techniques like XPS and XRD spectra which can be used to identify the location and chemical states of additives within the SnO_2. However, this approach requires multiple analytical procedures be conducted on each doped-SnO_2 sample after each processing step, particularly those involving heat treatments.

With respect to sensor design, both experimental and model developments are still vital. Studies, such as that conducted by Chowdhuri et al. [47] who found that patterned additives improved SnO_2 performance beyond that of randomly dispersed additives, point to promising possibilities. The incorporation of self-assembly methods into sensor fabrication, where self-assembly can be used to control additive patterning in the SnO_2, may improve both the sensor properties and reduce processing time and waste. Sensors with even more organized 3-dimensional micro/nano-architectures of additives in the SnO_2 sensing material may even further augment sensor performance beyond the results observed by Chowdhuri and co-workers in their surface patterning study. For example, the dependence of SnO_2 sensor performance on the bulk and microscale distribution and location of the additives suggests that functionally graded sensors (where the type of additive and the concentration change as a function of the location within the architecture of the sensor) may provide improved selectivity and discrimination between species when the sensor is exposed to a mixture of gases. Lastly, because the experimental data in the work by Cabot et al. [17, 24] and several others indicate additive morphology, distribution, chemical state, etc. affect sensor performance; models which incorporate these characteristics appear to be a vital next step in SnO_2 sensor design.

ACKNOWLEDGMENTS

The authors would like to acknowledge the generous support of the Office of the Vice Provost for Research at The University of Michigan and the National Defense Science and Engineering Graduate Fellowship program. This material is based upon work supported by the National Science Foundation under Grant No. 0329631.

REFERENCES

1. T. Seiyama, A. Kato, K. Fujiishi, and M. Nagatani, *Anal. Chem.* 34, 1502 (1962).
2. K. Ihokura and J. Watson, "The Stannic Oxide Gas Sensor—Principles and Applications." CRC Press, Boca Raton, FL, 1994.
3. N. Yamazoe, *Sens. Actuators B* 6, 9 (1992).
4. W. Göpel in "Sensors: A Comprehensive Survey" (Göpel, Hesse, and Zemel, Eds.), Weinheim: VCH, 1992.
5. V. M. Jiménez, A. R. González-Elipe, J. P. Espinós, A. Justo, and A. Fernández, *Sens. Actuators B* 31, 29 (1996).
6. W. Göpel and K. D. Schierbaum, *Sens. Actuators B* 26, 1 (1995)
7. N. Yamazoe, *Sens. Actuators B* 5, 7 (1991).
8. L. Hozer, translation editor D. Holland, "Semiconductor Ceramics: Grain Boundary Effects." Ellis Horwood, New York; PWN-Polish Scientific Publishers, Warsaw, 1994.
9. C. O. Park and S. A. Akbar, *J. Mater. Sci.* 38, 4611 (2003).
10. J. Calderer, P. Molinàs, J. Sueiras, E. Llobet, X. Vilanova, X. Correig, F. Masana, and A. Rodríguez, *Microelec. Rel.* 40, 807 (2000).
11. C. Xu, J. Tamaki, N. Miura, and N. Yamazoe, *Sens. Actuators B* 3, 147 (1991).
12. F. E. Krius, H. Fissan, and A. Peled, *J. Aerosol. Sci.* 29, 511 (1998).
13. G. Zhang and M. Liu, *Sens. Actuators B* 69, 144 (2000).
14. E. Kanazawa, M. Kugishima, K. Shimanoe, Y. Kanmura, Y. Teraoka, N. Miura, and N. Yamazoe, *Sens. Actuators B* 75, 121 (2001).
15. I. Sayago, J. Gutiérrez, L. Arés, J. I. Robla, M. C. Horrillo, J. Getino, J. Rino, and J. A. Agapito, *Sens. Actuators B* 26, 19 (1995).
16. P. Siciliano, *Sens. Actuators B* 70, 153 (2000).
17. A. Cabot, J. Arbiol, J. R. Morante, U. Weimar, N. Bârsan, and W. Göpel, *Sens. Actuators B* 70, 87 (2000).
18. N. Barsan and U. Weimar, *J. Electrocer.* 7, 143 (2001).
19. S. R. Morrison, *Sens. Actuators* 12, 425 (1987).
20. Y.-S. Choe, *Sens. Actuators B* 77, 200 (2001).
21. H. Ogawa, M. Nishikawa, and A. Abe, *J. Appl. Phys.* 53, 4448 (1982).
22. J. F. McAleer, P. T. Moseley, J. O. W. Norris, and D. E. Williams, *J. Chem. Soc. Faraday Trans.* 83, 1323, (1987).
23. P. Montmeat, J.-C. Marchand, R. Lalauze, J.-P. Viricelle, G. Tournier, and C. Pijolat, *Sens. Actuators B* 95, 83 (2003).
24. A. Cabot, A. Diéguez, A. Romano-Rodríguez, J. R. Morante, and N. Bârsan, *Sens. Actuators B* 79, 98 (2001).
25. C. G. Borman and R. G. Gordon, *J. Electrochem. Soc.* 136, 3820 (1989).
26. H. Unuma, H. Tahabatake, K. Watanabe, T. Ogata, and M. Sugawara, *J. Mater. Sci. Lett.* 21, 1241 (2002).
27. A. K. Mukhopadhyay, P. Mitra, A. P. Chatterjee, and H. S. Maiti, *Cer. Int.* 26, 123 (2000).
28. D. Lindackers, C. Janzen, B. Rellinghaus, E. F. Wassermann, and P. Roth, *Nanostruct. Mater.* 10, 1247 (1998).
29. W. Zhu and S. E. Pratsinis, *Cer. Process.* 43, 2657 (1997).
30. G. Skandan, N. Glumac, Y.-J. Chen, F. Cosandey, E. Heims, and B. H. Kear, *J. Amer. Cer. Soc.* 81, 2753 (1998).
31. L. M. Cukrov, T. Tsuzuki, and P. G. McCormick, *Scripta Mater.* 44, 1787 (2001).
32. N. Sergent, P. Gélin, L. Périer-Cambry, H. Praliaud, and G. Thomas, *Sens. Actuators B* 84, 176 (2002).
33. J. Zhang and L. Gao, *J. Solid State Chem.* 177, 1425 (2004).
34. N. S. Baik, G. Sakai, N. Miura, and N. Yamazoe, *Sens. Actuators B* 63, 74 (2000).
35. D. L. Hall, A. A. Wang, K. T. Joy, T. A. Miller, and M. S. Wooldridge, *J. Amer. Chem. Soc.* 87 (2004), in press.
36. N. S. Baik, G. Sakai, N. Miura, and N. Yamazoe, *Sens. Actuators B* 65, 97 (2000).
37. G. Sakai, N. S. Baik, N. Miura, and N. Yamazoe, *Sens. Actuators B* 77, 116 (2001).
38. M. S. Wooldridge, *Prog. Energy Combust. Sci.* 24, 63 (1998).
39. S. E. Pratsinis, *Prog. Energy Combust. Sci.* 24, 197 (1998).
40. J. S. Kim and M. A. Cappelli, *Surf. Coat. Tech.* 76–77, 791 (1995).
41. R. M. Laine, R. Baranwal, T. Hinklin, D. Treadwell, A. Sutorik, C. Bickmore, K. Waldner, and S. S. Neo, in "Novel Synthetic and Processing Routes to Ceramics" (Uematsu and H. Otsuka, Eds.), Vols. 159–160, p. 17. Key Engineering Materials, Trans. Tech. Publ. Ltd. Switzerland, 1998.

42. R. M. Laine, K. Waldner, C. Bickmore, and D. R. Treadwell, "Ultrafine Powders by Flame Spray Pyrolysis." U.S. Patent 5,958,361. 28, 1999.
43. G. Korotcenkov, V. Brinzari, V. Golovanov, and Y. Blinov, *Sens. Actuators B* 98, 41 (2004).
44. M. S. Wooldridge, P. V. Torek, D. L. Hall, T. R. Palmer, C. R. Schrock, T. A. Miller, and M. T. Donovan, *Combust. Flame* 131, 98 (2002).
45. B.-K. Min and S.-D. Choi, *Sens. Actuators B* 98, 239 (2004).
46. G. G. Mandayo, E. Castaño, F. J. Gracia, A. Cirera, A. Cornet, and J. R. Morante, *Sens. Actuators B* 95, 90 (2003).
47. A. Chowdhuri, V. Gupta, and K. Sreenivas, *IEEE Sens. J.* 3, 680 (2003).
48. J. Mizsei, L. Pirttiaho, M. Karppinen, and V. Lantto, *Sens. Actuators B* 65, 195 (2000).
49. G. Williams and G. S. V. Coles, *Sens. Actuators B* 24–25, 469 (1995).
50. M. Di Guilio, G. Micocci, A. Serra, A. Tepore, R. Rella, and P. Siciliano, *Sens. Actuators B* 24–25, 465 (1995).
51. M. Di Guilio, A. Serra, A. Tepore, R. Rella, P. Siciliano, and L. Mirenghi, *Mater. Sci. Forum* 203, 143 (1996).
52. M. C. Horrillo, A. Serventi, D. Rickerby, and J. Gutiérrez, *Sens. Actuators B* 58, 474 (1999).
53. Y. Nagasawa, K. Tabata, and H. Ohnishi, *Appl. Surf. Sci.* 121–122, 327 (1997).
54. S. Nicoletti, L. Dori, G. C. Cardinali, and A. Parisini, *Sens. Actuators B* 60, 90 (1999).
55. J.-M. Herrmann, J. Disdier, A. Fernández, V. M. Jiménez and J. C. Sánchez-López, *Nanostruct. Mater.* 8, 675 (1997).
56. M. K. Kennedy, F. E. Kruis, H. Fissan, B. R. Mehta, S. Stappert, and G. Dumpich, *J. App. Phys.* 93, 551 (2003).
57. M. Labeau, B. Gautheron, F. Cellier, M. Vallet-Regi, E. Garcia, and J.-M. Gonzàlez-Calbet, *J. Solid State Chem.* 102, 434 (1993).
58. A. Heilig, N. Barsan, U. Weimar, and W. Göpel, *Sens. Actuators B* 58, 302 (1999).
59. A. Chiorino, G. Ghiotti, F. Prinetto, M. C. Carotta, D. Gnani, and G. Martinelli, *Sens. Actuators B* 58, 338 (1999).
60. T. Brousse and D. M. Schleich, *Sens. Actuators B* 31, 77 (1996).
61. D. L. Hall, P. V. Torek, C. R. Schrock, T. R. Palmer, and M. S. Wooldridge, *Mater. Sci. Forum* 386, 347 (2002).
62. J. H. Sung, Y. S. Lee, J. W. Lim, Y. H. Hong, and D. D. Lee, *Sens. Actuators B* 66, 149 (2000).
63. K. C. Song and J. H. Kim, *Powder Tech.* 107, 268 (2000).
64. Y. Liu, W. Zhu, O. K. Tan, X. Yao, and Y. Shen, *J. Mater. Sci. Mater. Electron.* 7, 279 (1996).
65. G. N. Advani, Y. Komem, J. Hasenkopf, and A. G. Jordan, *Sens. Actuators* 2, 139 (1981/1982).
66. T. A. Miller, S. D. Bakrania, C. Perez, and M. S. Wooldridge, *J. Am. Cer. Soc.* (2004), in preparation for.
67. P. Ivanov, E. Llobet, X. Vilanova, J. Brezmes, J. Hubalek, and X. Correig, *Sens. Actuators B* 99, 201 (2004).
68. T. Takada, T. Fukunaga, and T. Maekawa, *Sens. Actuators B* 66, 22 (2000).
69. B. W. Licznerski, K. Nitsch, H. Teterycz, T. Sobañski, and K. Wiśniewski, *Sens. Actuators B* (2004), in press.
70. C. Bittencourt, E. Llobet, P. Ivanov, X. Correig, X. Vilanova, J. Brezmes, J. Hubalek, K. Malysz, J. J. Pireaux, and J. Calderer, *Sens. Actuators B* 97, 67 (2004).
71. R. E. Cavicchi, R. M. Walton, M. Aquino-Class, J. D. Allen, and B. Panchapakesan, *Sens. Actuators B* 77, 145 (2001).
72. N. S. Baik, N. Miura, and N. Yamazoe, *Sens. Actuators B* 77, 116 (2001).
73. L. M. Cukrov, P. G. McCormick, K. Galatsis, and W. Wlodarski, *Sens. Actuators B* 77, 491 (2001).